Electronic Supplementary Material (ESI) for Dalton Transactions.
This journal is © The Royal Society of Chemistry 2021

Supporting Information

Scrutinizing Ligand Exchange Reactions in the Formation of the Precious Group Metal-Organic Framework RuII,II-HKUST-1: The Impact of Diruthenium Tetracarboxylate Precursor and Modulator Choice

Werner R. Heinz,[a] Dominik Staude,[a] David Mayer,[a] Hana Bunzen,[b] and Roland A. Fischer[a,*]

[a] Chair of Inorganic and Metal-Organic Chemistry, Department of Chemistry, Technical University of Munich, Lichtenbergstraße 4, 85748 Garching, Germany. E-mail: roland.fischer@tum.de

[b] Chair of Solid State and Materials Chemistry, Institute of Physics, University of Augsburg, Universitätsstraße 1, 86159 Augsburg, Germany. E-mail: hana.bunzen@physik.uni-augsburg.de

Table of Contents

Experimental Details

General considerations

Trimesic acid (Sigma-Aldrich), $RuCl_3 \cdot x\ H_2O$ (Precious Metals Online) and HPLC-grade acetone and ethanol (VWR Chemicals) were purchased commercially and used without further purification. Substituted benzoic acid derivatives were purchased from Sigma-Aldrich (analytical grade) and used without further purification. 4-Methyl benzoic acid sodium salt was prepared by neutralization of the acid in aqueous NaOH and subsequent solvent removal. Ultra-pure water was obtained using a Milli-Q purification system (18.2 MΩ cm^{-1}). Dichloromethane, diethyl ether and tetrahydrofurane were purified and dried using a MBraun SPS-800 and additionally degassed and stored under argon atmosphere. All complexes and MOFs were synthesized under exclusion from air and handled in a using argon-filled (>99.996%; Westfalen) glovebox.

Instrumentation

Gloveboxes

MOF synthesis including degassed solvent and water were performed in an MBraun 500 glovebox operated under wet conditions in argon atmosphere. Activated MOF samples were stored and handled in another glovebox under dry Ar atmosphere conditions.

Powder X-Ray diffraction

All diffraction patterns were collected on a PANalytical Empyrean equipped with a Cu X-ray tube (λ = 0.154 nm) operated at 45 kV and 40 mA in a 2Θ range of 5-50° in steps of 0.0065651° (2Θ) with 0.175 s/step. The incident beam was focussed on the sample through a focusing beam mirror with a 1/8° divergence slit and a nickel beta filter (0.2 mm). A PIXcel1D detector was used in receiving mode with a 1/8° anti-scatter slit and 0.04 rad soller slits. The activated MOF samples and dried precursor adducts were filled in borosilicate capillaries of 0.5 mm inner diameter and mounted onto a capillary spinner. Free carboxylic acid reference spectra were measured with reflection-transmission-spinner (RTS) mode.

Single crystal X-Ray diffraction

Single crystal structures of related precursor complexes were either measured on a Bruker D8 Venture diffractometer equipped with a Helios optic monochromator, a Photon 100 CMOS detector and a Mo IMS microsource (λ = 0.71073 Å), or on a Bruker D8 Venture diffractometer equipped with a Helios optic monochromator, a Photon 100 CMOS detector and a Mo rotating anode source (λ = 0.71073 Å), at 100(2) K. The raw area detector data frames were reduced and corrected for absorption effects using the SAINT and SADABS programs with multi-scan absorption correction. Final unit cell parameters were determined by least-squares refinement of the respective independent reflections taken from the data sets. The structures were solved by intrinsic phasing with SHELXT. Difference Fourier calculations and full-matrix least-squares refinements against F^2 were performed by SHELXL-2014/7 (Sheldrick, 2014). All non-hydrogen atoms were refined with anisotropic displacement parameters. Hydrogen atoms throughout could not be located in the Fourier maps and were calculated in ideal positions using a riding model (d(C-H) = 0.95 Å, $U_{ISO}(H) = U_{EQ}(C)$). Disordered solvent molecules, which could not properly be refined were treated as diffuse contribution to the overall scattering without specific positions using the Squeeze routine in Platon. Single crystals were directly taken from the reaction solution and fixed on microsampler using perfluorated ether under an Ar counterflow. Crystal structure graphics were created using Mercury software.

Elemental Analysis

Determination of the elemental composition was performed together with the microanalytical laboratories of the chemistry department at the Technical University of Munich. Determination of C, H, N and S was carried out with a Hekatech EuroEA elemental analyser with samples of 1-3 mg. Samples were decomposed at T >1000 °C in oxygen atmosphere and decomposition gases purified and separated through a GC column. Detection and quantification of CO_2, H_2O, NO_2 and SO_2 allowed to derive elemental contents. Metal contents were derived from TGA-based metal oxide residues as reported earlier.[1] Low sample amounts obstructed the analysis of F contents in OBz-F and OBz-CF_3 samples.

Gas sorption measurements

Sorption experiments were conducted using a *Micromeritics 3Flex* with each ~50 mg of desolvated sample. Prior to the measurement each sample was additionally degassed at 150°C for >10h. Nitrogen isotherms were recorded at 77 K. The BET surface area was calculated using data points in the relative pressure range of 0.01 to 0.1 in the adsorption branch with the *Rouquerol* consistency criteria considered.

Fourier-transform infrared spectroscopy

FT-IR spectra were recorded from finely ground activated powder samples under argon atmosphere in a glovebox using a *Bruker ALPHA* FTIR spectrometer equipped with a Pt attenuated total reflectance (ATR) unit at room temperature in the range of 400 to 4000 cm^{-1} with a resolution of 2 cm^{-1} and 24 scans per measurement. A pyroelectric deuterated L-alanine doped triglycine sulfate (RT-DLaTGS) detector was used.

Raman spectroscopy

Raman spectroscopy was measured with an inVia Reflex Raman System with an optical microscope (Leica DM2700M, 50x magnification) coupled to a *Renishaw R04* Raman spectrometer with 532 nm laser wavelength (Laser: RL532C, Class 3B) with activated samples filled into Borosilicate glass capillaries (0.5 mm inner diameter) under argon atmosphere. A Renishaw 266n10 detector was used. All samples were measured with 10 s exposure time, 1 % laser power and 10 accumulations.

NMR spectroscopy

Standard liquid ^{1}H-NMR spectra were recorded with a *Bruker AV400US* at 400 MHz at 298 K. Kinetic measurements and ^{19}F-NMR were measured using a *Bruker DRX400* (400 MHz) with implemented heating module at 298 K unless otherwise stated. Sensitive samples were prepared using degassed deuterated solvents. MestreNova was used for data analysis applying manual phase correction and automated baseline correction (Whittaker Smoother). Chemical shifts are given in parts per million (ppm) and calibrated to the residual proton signal of the deuterated solvent. Multiplicity is given as s – singlet as paramagnetic ruthenium accounts for significant line broadening.

LIFDI mass spectrometry

Liquid injection field desorption ionization mass spectrometry was measured on a *Waters LCT Micromass* TOF MS with additional LIFDI module using a current of 80 mA for sample evaporation. Prior to measurements, dissolved samples were filtered through 0.2 µm syringe filter (PTFE). Instrument control and data analysis was performed using *MassLynx NT* software package.

Thermogravimetric analysis

Thermal analysis of the materials was determined with a Mettler Toledo TGA/DSC 3+ in aluminium oxide crucibles (70 µL with lid) with sample amounts of 1 to 5 mg. Samples of activated materials were taken under inert conditions in a glovebox and transferred to the measurement chamber in screw capped vials immediately prior to the measurement. The following thermal program was applied using

synthetic air (20 mL min^{-1}, Westfalen, 80% N_2; 20% O_2): At 30 °C isothermal equilibration (15 min), ramp from 30 °C to 700 °C with 10 K min^{-1}, at 700 °C isothermal equilibration (15 min).

High-resolution transmission electron microscopy

TEM and STEM micrographs and EDS elemental mappings were recorded with a JEM NEOARM microscope (JEOL) with a cold FEG electron source operated at 200 kV. Samples were prepared by depositing a drop of the crystalline products dispersed in ethanol onto carbon-coated copper grids (200 mesh) and dried in air.

Synthesis of Precursor Complexes

All syntheses were performed under exclusion from air and with degassed solvents and solutions. The obtained powders crystallize as adducts coordinating two solvent molecules (THF or acetone) on the axial positions of the PW. XRD measurements were performed with these adducts, while all other characterizations (yield, NMR, IR, EA) were performed with the amorphized desolvated complexes after thermal activation at 80 °C for 12 h. Reaction yields of isolated complexes refer to $RuCl_3$ assumed as dihydrate.

General Procedure via the “blue solutions of ruthenium (II)

Acetate and benzoate precursor complexes were synthesized according to literature procedures via the “blue solutions” of Ru^{2+} with slight modifications.[2] The blue solutions were prepared in a *Fisher Porter* bottle using carefully degassed dispersions of $RuCl_3 \cdot x\ H_2O$ (1-3 g, 1.0 eq.) and PtO_2 (17.9 mg) in MeOH (10-30 mL). The black mixtures were stirred for 3 h under hydrogen atmosphere (3 bar). The resulting deep blue solution was filtered through a Schlenk frit into a solution of the respective carboxylic acid alkali metal salt (2.5-2.8 eq for sodium benzoates, 5.8 eq for lithium acetate) in MeOH (10-30 mL). The whole mixture was heated to reflux for 24 h. Workup of the $Ru_2(OAc)_4$ was performed by removal of the supernatant by *Whatman* filtration and successive drying of the formed microcrystalline powder in argon stream. Workup of methyl benzoate and methoxy benzoate complexes was achieved by an additional washing step of the precipitate with hot MeOH. All other diruthenium tetrabenzoate complexes were isolated by removal of the solvent in vacuo and subsequent extraction with hot acetone, concentration of the extract, and crystallisation at -32 °C.

Additional Information – Precursor Characterization

Diruthenium tetraacetate

$Ru_2(OAc)_4$ was synthesized according to above-mentioned modified literature procedure.[2] Yield: 43 % of a brown powder. ^{1}H-NMR: (400 MHz, THF-d^8, 298 K): δ [ppm] = 1.09 (s, 12H, CH_3); EA: (calc / found %): C (21.9/21.3), H (2.76/2.68); LIFDI-MS (THF): (calc/found) m/z = (438.32/438.68).

Diruthenium tetrabenzoate

$Ru_2(OBz)_4$ was synthesized according to above-mentioned modified literature procedure.[2] Yield: 17 % of a brown powder. ^{1}H-NMR: (400 MHz, THF-d^8, 298 K): δ [ppm] = 16.50 (s, 8H, *ortho*-H), 10.71 (s, 4H, *para*-H), 9.26 (s, 8H, *meta*-H); EA: (calc / found %): C (49.0/49.0), H (2.94/3.00); LIFDI-MS (THF): (calc/found) m/z = (686.6/687.1).

Diruthenium tetra (4-fluoro benzoate)

$Ru_2(OBz\text{-}F)_4$ was synthesized according to above-mentioned modified literature procedure.[2] Yield: 40 % of a dark brown powder. ^{1}H-NMR: (400 MHz, THF-d^8, 298 K): δ [ppm] = 16.47 (s, 8H, *ortho*-H), 9.00 (s, 8H, *meta*-H); EA: (calc / found %): C (44.3/43.5), H (2.13/2.15); LIFDI-MS (THF): (calc/found) m/z = (758.6/759.6).

Diruthenium tetrakis (4-trifluoromethyl benzoate)

$Ru_2(OBz\text{-}CF_3)_4$ was synthesized according to above-mentioned modified literature procedure.[2] Yield: 18 % of an orange powder. ^{1}H-NMR: (400 MHz, THF-d^8, 298 K): δ [ppm] = 16.63 (s, 8H, *ortho*-H), 9.64 (s, 8H, *meta*-H); EA: (calc / found %): C (40.1/39.9), H (1.68/1.64); LIFDI-MS (THF): (calc/found) m/z = (958.6/959.9).

Diruthenium tetra (4-methyl benzoate)

$Ru_2(OBz\text{-}Me)_4$ was synthesized according to above-mentioned modified literature procedure.[2] Yield: 47 % of a light brown powder. ^{1}H-NMR: (400 MHz, THF-d^8, 298 K): δ [ppm] = 16.45 (s, 8H, *ortho*-H), 9.20 (s, 8H, *meta*-H) 2.96 (s, 12H, CH_3); EA: (calc / found %): C (51.8/50.0), H (3.80/3.76); LIFDI-MS (THF): (calc/found) m/z = (742.7/743.1).

Diruthenium tetra (4-methoxy benzoate)

$Ru_2(OBz\text{-}OMe)_4$ was synthesized adopting the above-mentioned procedure. Yield: 34 % of a brown powder. ^{1}H-NMR: (400 MHz, THF-d^8, 298 K): δ [ppm] = 16.66 (s, 8H, *ortho*-H), 8.75 (s, 8H, *meta*-H) 4.79 (s, 12H, OCH_3); EA: (calc / found %): C (47.6/45.4), H (3.50/3.32).

Diruthenium tetrakis (3,5-dimethoxy benzoate)

$Ru_2(OBz\text{-}(OMe)_2)_4$ was synthesized by adopting the above-mentioned procedure via the blue solutions. Yield: 34 % of a light brown powder (86% purity according to NMR and 14% free acid impurity). ^{1}H-NMR: (400 MHz, THF-d^8, 298 K): δ [ppm] = 15.53 (s, 8H, *ortho*-H), 9.63 (s, 4H, *para*-H) 4.69 (s, 24H, OCH_3); EA: (calc / found %): C (46.7/45.2), H (3.92/3.82).

Diruthenium tetraacetate chloride

$Ru_2(OAc)_4Cl$ was synthesized according to modified literature procedures.[3] A mixture of $RuCl_3 \cdot x\ H_2O$ (7.5 g, 28.7 mmol, 1.0 eq.) and LiCl (7.5 g, XX mmol, XX eq), acetic acid (190 mL) and acetic anhydride (100 mL) was degassed by a stream of argon over 30 min and subsequently heated to reflux for 3 d in argon atmosphere. After cooldown to ambient temperature, the red brown precipitate was collected by filtration in air. The crude product was washed with cold acetone until the washing solution remained colorless and subsequently dried in vacuo. Yield: 73 % of a red brown powder. EA: (calc / found %): C (20.3/20.1), H (2.55/2.49).

Diruthenium tetra (L-mandelate)

$Ru_2(mand)_4$ was synthesized according to a literature procedure.[4] $Ru_2(OAc)_4Cl$ (202 mg, 0.43 mmol, 1 eq.) and L-mandelic acid (1.6 g, 10.52 mmol, 24 eq.) were dissolved in H_2O (125 mL) and heated to reflux for 90 min. The resulting yellow green solution was slowly cooled down to 4 °C. After 8 d, the supernatant was removed via *Whatman* filtration and the golden microcrystalline powder carefully dried under reduced pressure. After sampling for PXRD, the remaining solid was desolvated at 80 °C for 60 h. Yield: 21 % of a golden powder. ^{1}H-NMR: (400 MHz, CD_3CN, 298 K): δ [ppm] = 14.30 (s, 8H, *ortho*-H), 11.50 (s, 4H, *para*-H) 9.91 (s, 8H, *meta*-H) 9.48 (s, 4H, CH_{aliph}) 9.19 (s, 4H, OH); EA: (calc / found %): C (47.6/46.1), H (3.50/3.34).

PXRD

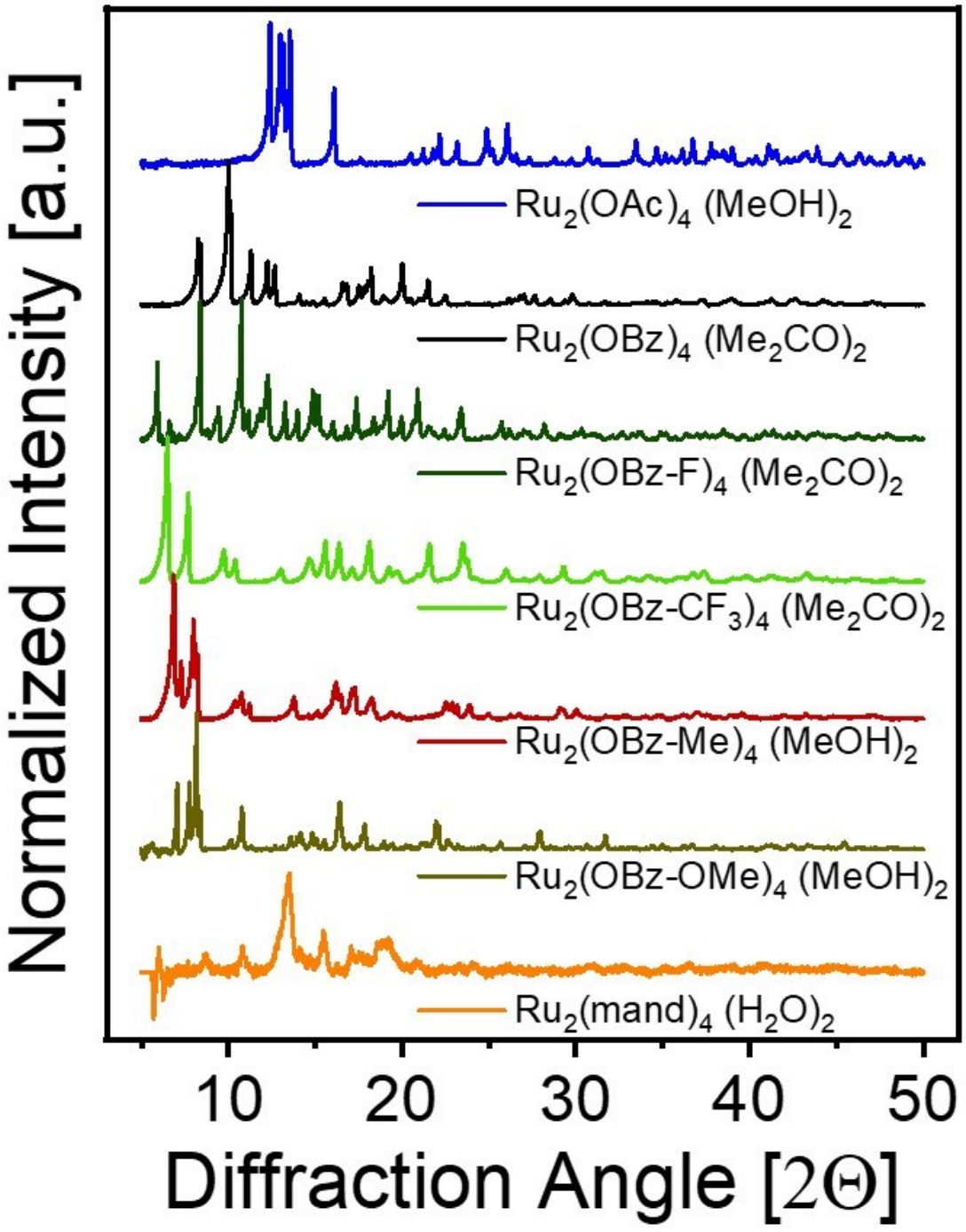

Figure S 1: Background-corrected and normalized PXRD pattern of the obtained univalent Ru-PW precursor adducts of methanol, water or acetone as indicated. Note that, low signal intensity and instrumental reasons caused a negative baseline for $Ru_2(mand)_4 (H_2O)_2$ sample. Precursors were desolvated prior to usage in MOF syntheses.

FT-IR spectra

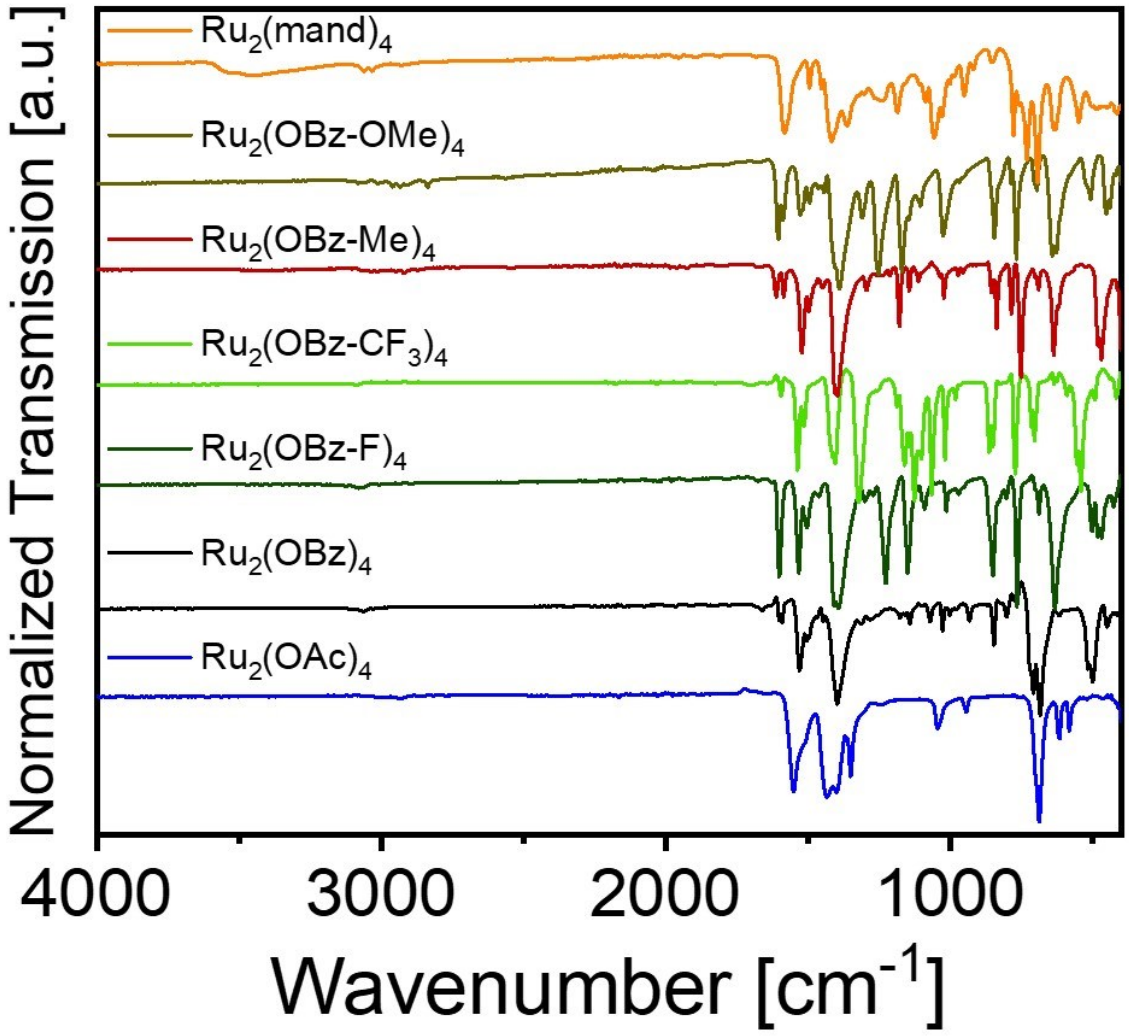

Figure S 2: Stacked and normalized FT-IR spectra of the Ru-PW precursors complexes used for MOF syntheses.

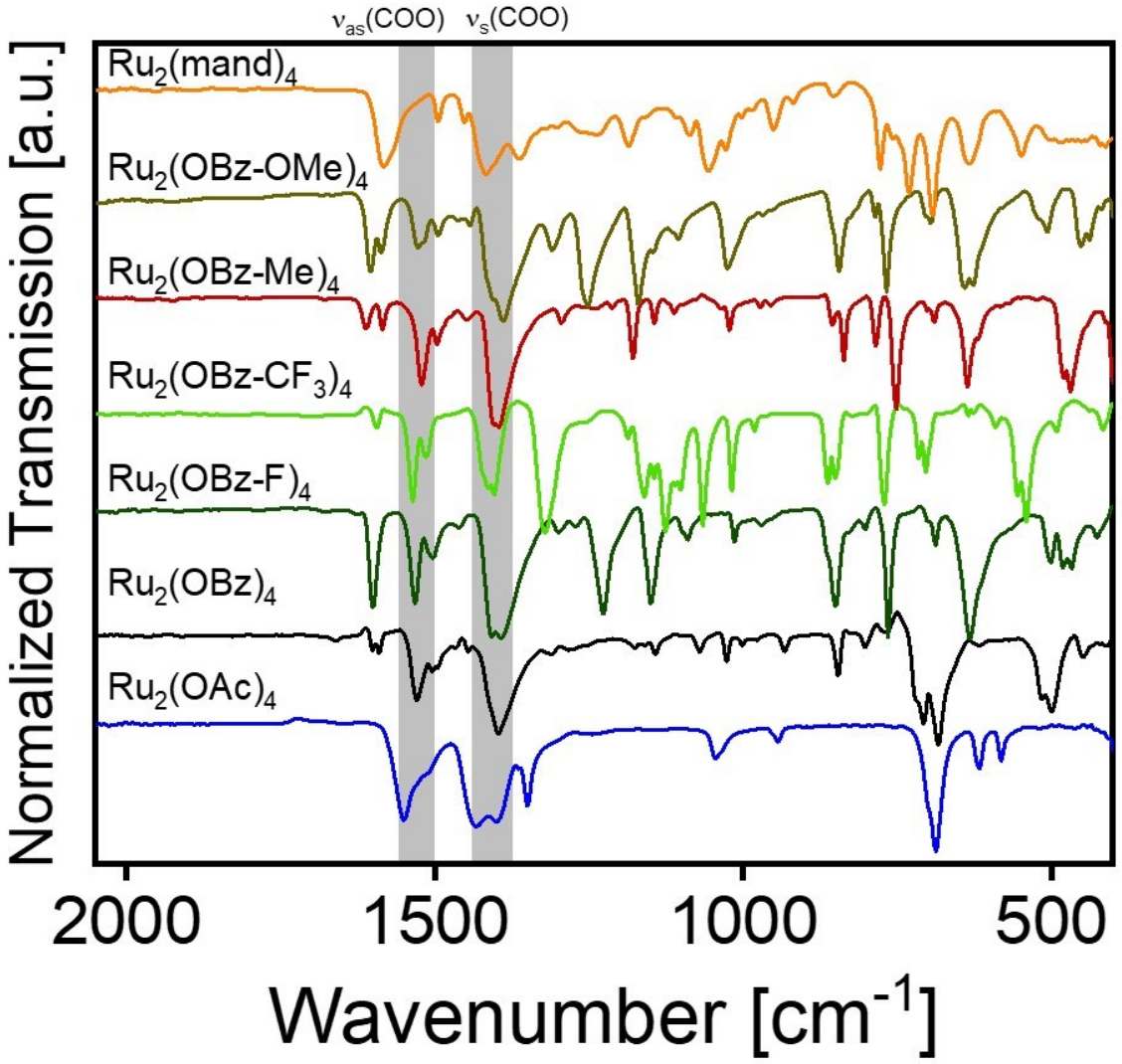

Figure S 3: Selected region (2000-400 cm^{-1}) of FT-IR spectra of the univalent Ru-PW precursor complexes. The highlighted regions indicate the asymmetric and symmetric carboxylate stretch vibrations indicating the +II / +II valency. Note that, apparently the adjacent hydroxy side groups of the ruthenium mandelate precursor cause a blue shift of ν_{as}(COO) towards absorption at 1583 cm^{-1}.

SC-XRD Structures

Single crystal X-ray crystallography of the diruthenium(II,II) tetra-μ-carboxylate paddlewheel complexes were mainly affected by their crystallization behavior (solubility issues) and their air sensitivity, which required single crystal search under inert conditions. All single crystals were directly taken from the respective reaction solutions, which were slowly cooled to -32 °C. The compounds throughout tend to crystallize as small plates or long needles, showing a crystallization behavior to form multiple stacking layers. Thus, the compounds showed a pronounced tendency to form twinned structures. For each compound, we therefore tested a couple of different single crystals until good quality for a full subsequent measurement was achieved. For the compound $Ru_2(OBz\text{-}CF_3)_4(THF)_2$, however, we were not able to improve the crystallization protocol in a way to achieve higher-quality crystals, showing less intergrowth behavior. We, nevertheless, were able to achieve a structure model of the paddlewheel complex by SC-XRD analysis, which showed sufficient quality for discussion of bond-lengths, angles etc. to be compared to the other complexes. For the sake of completeness and as further characterization detail, we here are providing the found structure model (crystal system, atom coordinates).

$Ru_2(OBz\text{-}CF_3)_4(THF)_2$

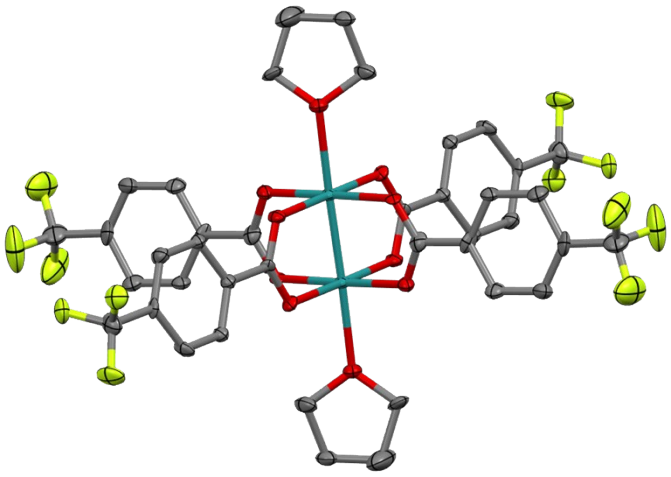

Figure S 4: ORTEP representation of $Ru_2(OBz\text{-}CF_3)_4(Me_2CO)_2$ with 50% probability level.

Table S 1: SC-XRD data of the complex $Ru_2(OBz\text{-}CF_3)_4(Me_2CO)_2$.

compound	**$Ru_2(OBz\text{-}CF_3)_4(Me_2CO)_2$**
Formula	$C_{40}\,H_{32}\,F_6\,O_{10}\,Ru_2$
Formula weight	1112.80
Temperature (K)	100(2)
Wavelength (Å)	0.7103 (Mo-K_α)

Crystal system	monoclinic
Space group	C 1 2/c 1
Z	8
a (Å)	24.756(6)
b (Å)	14.090(3)
c (Å)	16.243(3)
α (°)	90
β (°)	110.200(7)
γ (°)	90
Volume (Å^3)	5317(2)

Symbol	x/a	y/b	z/c	U
Ru1	0.53315(2)	0.48847(5)	0.56760(3)	0.0141836
F1	0.3338(3)	-0.0114(6)	0.6468(4)	0.072389
F2	0.2741(3)	0.0049(6)	0.5197(3)	0.0734417
F3	0.2671(3)	0.0914(6)	0.6233(4)	0.0783953
F4	0.25209(19)	0.8500(5)	0.6684(3)	0.0394186
F5	0.32436(19)	0.8656(4)	0.7884(3)	0.0351291
F6	0.27172(17)	0.7412(4)	0.7674(3)	0.0351291
O1	0.48884(19)	0.3710(5)	0.5830(3)	0.020146
O2	0.42380(18)	0.3908(4)	0.4491(2)	0.0171187
O3	0.48374(19)	0.5681(4)	0.6207(3)	0.0191009
O4	0.4186(2)	0.5927(4)	0.4874(3)	0.0194071
O5	0.6020(2)	0.4711(5)	0.7046(3)	0.0218944
C1	0.3037(4)	0.0546(9)	0.5892(5)	0.0420945
C2	0.3418(3)	0.1274(8)	0.5718(5)	0.0343539
C3	0.3968(3)	0.1420(8)	0.6284(5)	0.0328046
H3	0.41171	0.10435	0.67980	0.039
C4	0.4300(3)	0.2102(7)	0.6109(4)	0.025048
H4	0.46873	0.21784	0.64896	0.03
C5	0.4078(3)	0.2701(6)	0.5368(4)	0.0200749
C6	0.3522(3)	0.2553(7)	0.4792(4)	0.0230204
H6	0.33732	0.29390	0.42831	0.027
C7	0.3180(3)	0.1844(8)	0.4954(4)	0.0307509
H7	0.27978	0.17423	0.45639	0.037
C8	0.4431(3)	0.3502(7)	0.5224(4)	0.0228942
C9	0.2953(4)	0.8053(8)	0.7260(5)	0.0328228
C10	0.3335(3)	0.7524(6)	0.6859(4)	0.0180736
C11	0.3809(3)	0.7068(7)	0.7378(4)	0.0241645
H11	0.39064	0.70837	0.79974	0.029
C12	0.4156(3)	0.6571(6)	0.7007(4)	0.0172297
H12	0.44897	0.62434	0.73663	0.021

C13	0.4002(3)	0.6566(6)	0.6096(4)	0.0171747
C14	0.3523(3)	0.7031(6)	0.5577(4)	0.0179712
H14	0.34192	0.70035	0.49568	0.021
C15	0.3184(3)	0.7543(7)	0.5942(4)	0.0219123
H15	0.28606	0.78942	0.55847	0.021
C16	0.4366(3)	0.6013(6)	0.5693(4)	0.0140649
C17	0.5974(3)	0.4089(7)	0.7713(4)	0.0283364
H17A	0.58244	0.34613	0.74623	0.034
H17B	0.57110	0.43588	0.79938	0.034
C18	0.6571(4)	0.3999(11)	0.8364(5)	0.0667195
H18A	0.65737	0.41397	0.89624	0.08
H18B	0.67179	0.33473	0.83564	0.08
C19	0.6933(3)	0.4697(7)	0.8101(4)	0.0304985
H19A	0.73270	0.44501	0.82191	0.037
H19B	0.69558	0.53089	0.84111	0.037
C20	0.6615(3)	0.4803(8)	0.7135(4)	0.0342819
H20A	0.66914	0.54309	0.69241	0.041
H20B	0.67295	0.43010	0.68008	0.041

Atom1	Atom2	Length
Ru1	O1	2.048(7)
Ru1	O3	2.056(6)
Ru1	O5	2.302(4)
F1	C1	1.35(1)
F2	C1	1.32(1)
F3	C1	1.32(1)
F4	C9	1.31(1)
F5	C9	1.33(1)
F6	C9	1.37(1)
O1	C8	1.252(7)
O2	C8	1.257(8)
O3	C16	1.267(8)
O4	C16	1.254(8)
O5	C17	1.43(1)
O5	C20	1.435(9)
C1	C2	1.49(2)
C2	C3	1.370(9)
C2	C7	1.42(1)
C3	H3	0.950
C3	C4	1.36(1)
C4	H4	0.951
C4	C5	1.42(1)
C5	C6	1.387(9)
C5	C8	1.49(1)
C6	H6	0.951
C6	C7	1.39(1)
C7	H7	0.950
C9	C10	1.52(1)

C10	C11	1.35(1)
C10	C15	1.405(9)
C11	H11	0.950
C11	C12	1.40(1)
C12	H12	0.950
C12	C13	1.395(9)
C13	C14	1.362(9)
C13	C16	1.50(1)
C14	H14	0.951
C14	C15	1.39(1)
C15	H15	0.950
C17	H17A	0.990
C17	H17B	0.991
C17	C18	1.50(1)
C18	H18A	0.990
C18	H18B	0.99
C18	C19	1.49(2)
C19	H19A	0.990
C19	H19B	0.990
C19	C20	1.500(8)
C20	H20A	0.99
C20	H20B	0.99

$Ru_2(OBz\text{-}Me)_4(Me_2CO)_2$

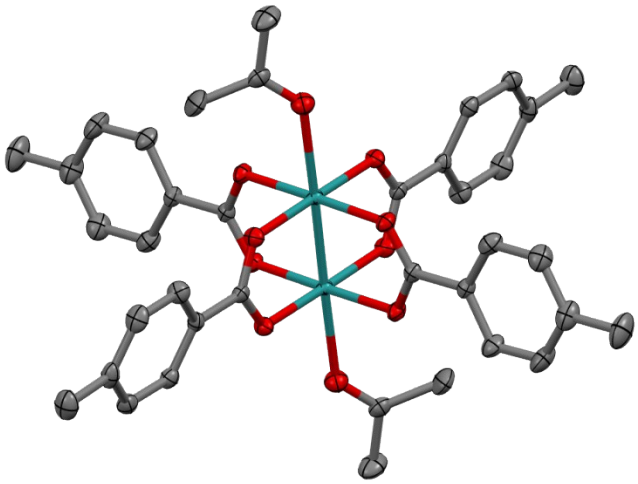

Figure S 5: ORTEP representation of $Ru_2(OBz\text{-}Me)_4(Me_2CO)_2$ with 50% probability level.

Table S 2: SC-XRD data of the complex $Ru_2(OBz\text{-}Me)_4(Me_2CO)_2$.

Compound	**$Ru_2(OBz\text{-}Me)_4(Me_2CO)_2$**
Formula	$C_{38}H_{40}O_{10}Ru_2$
CCDC	2043844
Formula weight	858.84
Temperature (K)	100(2)
Wavelength (Å)	0.7103 (Mo-K_α)
Crystal system	triclinic
Space group	P -1
Z	1
a (Å)	6.6721(13)
b (Å)	11.701(2)
c (Å)	12.113(2)
α (°)	96.337(8)
β (°)	104.603(8)
γ (°)	103.407(8)

Volume (Å^3)	875.7(3)
μ (mm^{-1})	0.921
d_{calc} (g/cm^3)	1.629
F (000)	436
Crystal size (mm^3)	0.045x 0.133 x 0.280
Theta range	2.30° to 25.35°
Index range	-8 ≤ h ≤ 8
	-14 ≤ k ≤ 14
	-14 ≤ l ≤ 14
Refl. collected	34266
Independent reflections	3196 (R_{int} = 0.1059)
Data/restraints/parameters	3195 / 0 / 230
GOF on F^2	1.034
R_1/wR_2[a]	0.0425 / 0.1172
[I ≥ 2σ(I)][b]	
R_1/wR_2	0.0487 / 0.1218
[all data]	
Largest diff. peak and hole	1.642 and -0.757 eÅ^{-3}

a: $w = 1/\left[\sigma^2\left(F_o^2\right) + (0.0733P)^2 + 2.19991P\right]$ where $P = (F_o^2 + 2F_c^2)/3$

b: $R_1 = \sum \| F_o| - |F_c \| / \sum |F_o|$; $wR_2 = \{\sum [w\left(F_o^2 - F_c^2\right)^2] / \sum [w(F_o^2)^2]\}^{1/2}$

Atom1	Atom2	Length
Ru1	O1	2.056(3)
Ru1	O3	2.047(4)
Ru1	O5	2.350(4)
O1	C1	1.274(5)
O2	C1	1.247(6)
O3	C9	1.256(5)
O4	C9	1.271(6)
O5	C18	1.205(6)
C1	C2	1.475(7)
C2	C3	1.387(7)
C2	C7	1.380(6)
C3	C4	1.373(7)
C3	H3	0.950

C4	C5	1.390(8)
C4	H4	0.950
C5	C6	1.392(7)
C5	C8	1.495(7)
C6	C7	1.376(7)
C6	H6	0.951
C7	H7	0.950
C8	H8A	0.980
C8	H8B	0.980
C8	H8C	0.980
C9	C10	1.483(7)
C10	C11	1.393(8)
C10	C15	1.384(6)
C11	C12	1.368(8)
C11	H11	0.950
C12	C13	1.381(7)
C12	H12	0.949
C13	C14	1.390(9)
C13	C16	1.501(9)
C14	C15	1.371(8)
C14	H14	0.950
C15	H15	0.950
C16	H16A	0.980
C16	H16B	0.979
C16	H16C	0.980
C17	C18	1.486(9)
C17	H17A	0.981
C17	H17B	0.980
C17	H17C	0.980
C18	C19	1.483(8)
C19	H19A	0.980
C19	H19B	0.981
C19	H19C	0.979

$Ru_2(OBz\text{-}OMe)_4(Me_2CO)_2$

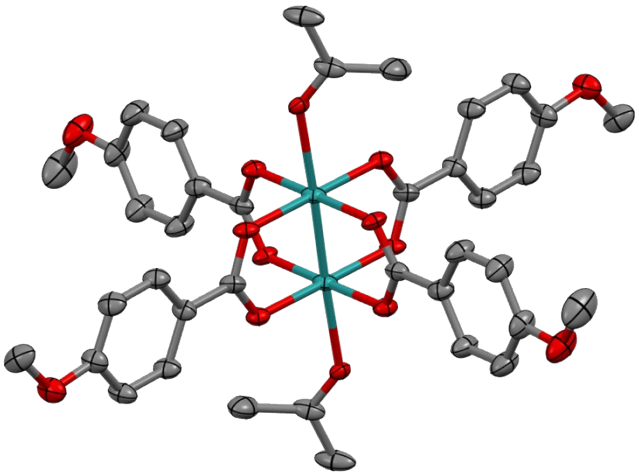

Figure S 6: ORTEP representation of $Ru_2(OBz\text{-}OMe)_4(Me_2CO)_2$ with 50% probability level.

Table S 3: SC-XRD data of the complex $Ru_2(OBz\text{-}OMe)_4(Me_2CO)_2$.

Compound	**$Ru_2(OBz\text{-}OMe)_4(Me_2CO)_2$**
Formula	$C_{38}H_{40}O_{14}Ru_2$
CCDC	2043845
Formula weight	922.84
Temperature (K)	100(2)
Wavelength (Å)	0.7103 (Mo-K_α)
Crystal system	monoclinic
Space group	C 1 2/c 1
Z	4
a (Å)	24.3485(18)
b (Å)	9.9212(7)
c (Å)	23.6907(11)
α (°)	90
β (°)	117.401(2)
γ (°)	90

Volume (Å^3)	5080.8(6)
μ (mm^{-1})	0.645
d_{calc} (g/cm^3)	1.206
F (000)	1827
Crystal size (mm^3)	0.049 x 0.175 x 0.365
Theta range	2.26° to 25.35°
Index range	-29 ≤ h ≤ 29
	-11 ≤ k ≤ 11
	-28 ≤ l ≤ 28
Refl. collected	101964
Independent reflections	4638 (R_{int} = 0.0802)
Data/restraints/parameters	4638 / 0 / 244
GOF on F^2	1.197
R_1/wR_2[a]	0.0574 / 0.1190
[I ≥ 2σ(I)][b]	
R_1/wR_2	0.0690 / 0.1258
[all data]	
Largest diff. peak and hole	1.366 and -1.107 eÅ^{-3}

a: $w = 1/\left[\sigma^2\left(F_o^2\right) + 71.3381P\right]$ where $P = (F_o^2 + 2F_c^2)/3$

b: $R_1 = \sum \| F_o| - |F_c \| / \sum |F_o|$; $wR_2 = \{\sum [w\left(F_o^2 - F_c^2\right)^2] / \sum [w(F_o^2)^2]\}^{1/2}$

Atom1	Atom2	Length
Ru1	O1	2.057(4)
Ru1	O4	2.047(4)
Ru1	O7	2.342(3)
O1	C1	1.266(6)
O2	C1	1.280(8)
O3	C5	1.359(8)
O3	C8	1.434(7)
O4	C9	1.264(8)
O5	C9	1.275(6)
O6	C13	1.352(9)
O6	C16	1.416(8)
O7	C18	1.218(6)
C1	C2	1.479(8)

C2	C3	1.394(8)
C2	C7	1.397(9)
C3	C4	1.38(1)
C3	H3	0.950
C4	C5	1.38(1)
C4	H4	0.950
C5	C6	1.391(8)
C6	C7	1.38(1)
C6	H6	0.951
C7	H7	0.950
C8	H8A	0.981
C8	H8B	0.980
C8	H8C	0.979
C9	C10	1.49(1)
C10	C11	1.39(1)
C10	C15	1.394(8)
C11	C12	1.38(1)
C11	H11	0.950
C12	C13	1.394(8)
C12	H12	0.949
C13	C14	1.38(1)
C14	C15	1.36(1)
C14	H14	0.951
C15	H15	0.949
C16	H16A	0.979
C16	H16B	0.98
C16	H16C	0.979
C17	C18	1.494(8)
C17	H17A	0.980
C17	H17B	0.979
C17	H17C	0.979
C18	C19	1.492(9)
C19	H19A	0.979
C19	H19B	0.98
C19	H19C	0.980

$Ru_2(OBz\text{-}(OMe)_2)_4(Me_2CO)_2$

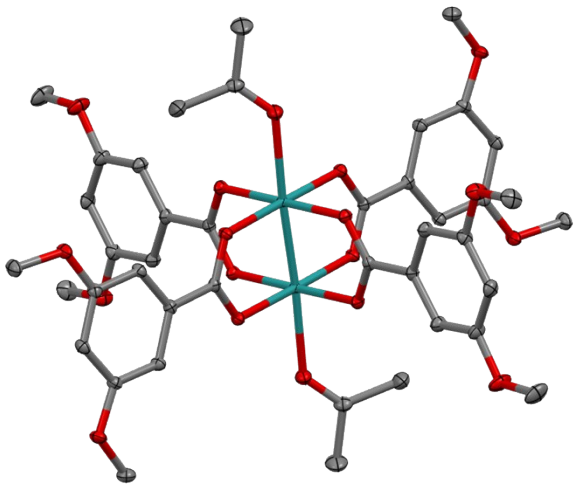

Figure S 7: ORTEP representation of $Ru_2(OBz\text{-}(OMe)_2)_4(Me_2CO)_2$ with 50% probability level.

Table S 4: SC-XRD data of the complex $Ru_2(OBz\text{-}(OMe)_2)_4(Me_2CO)_2$.

Compound	**$Ru_2(OBz\text{-}(OMe)_2)_4(Me_2CO)_2$**
Formula	$C_{48}H_{60}O_{20}Ru_2$
CCDC	2043847
Formula weight	1159.10
Temperature (K)	100(2)
Wavelength (Å)	0.7103 (Mo-K_α)
Crystal system	triclinic
Space group	P -1
Z	1
a (Å)	9.6301(5)
b (Å)	11.2950(6)
c (Å)	12.4945(6)
α (°)	99.576(2)
β (°)	107.789(2)
γ (°)	97.983(2)
Volume (Å^3)	1249.72(11)

μ (mm^{-1})	0.682
d_{calc} (g/cm^3)	1.540
F (000)	596
Crystal size (mm^3)	0.068 x 0.110 x 0.176
Theta range	2.26° to 30.56°
Index range	-13 ≤ h ≤ 13
	-16 ≤ k ≤ 16
	-17 ≤ l ≤ 17
Refl. collected	7602
Independent reflections	7096 (R_{int} = 0.0144)
Data/restraints/parameters	7602 / 6 / 334
GOF on F^2	1.037
R_1/wR_2[a]	0.0224 / 0.0544
[I ≥ 2σ(I)][b]	
R_1/wR_2	0.0198 / 0.0529
[all data]	
Largest diff. peak and hole	0.071 and -0.894 $eÅ^{-3}$

a: $w = 1/\left[\sigma^2\left(F_o^2\right) + (0.0306P)^2 + 0.0689P\right]$ where $P = (F_o^2 + 2F_c^2)/3$

b: $R_1 = \sum \| F_o| - |F_c \| / \sum |F_o|$; $wR_2 = \{\sum [w\left(F_o^2 - F_c^2\right)^2] / \sum [w(F_o^2)^2]\}^{1/2}$

Atom1	Atom2	Length
Ru1	O1	2.0566(7)
Ru1	O3	2.0645(9)
Ru1	O5	2.335(1)
O1	C1	1.273(2)
C1	O2	1.267(1)
C1	C2	1.493(1)
C2	C3	1.394(2)
C2	C7	1.392(2)
O3	C10	1.267(2)
C3	H3	0.950
C3	C4	1.394(1)
O4	C10	1.271(2)
C4	C5	1.396(2)
C4	O7	1.366(2)
O5	C19	1.223(2)

C5	H5	0.950
C5	C6	1.396(2)
O6	C6	1.365(2)
O6	C8	1.427(1)
C6	C7	1.387(1)
O7	C9	1.426(1)
C7	H7	0.950
O8	C15	1.363(2)
O8	C18	1.432(2)
C8	H8A	0.980
C8	H8AB	0.980
C8	H8AC	0.980
O9	C13	1.365(2)
O9	C17	1.430(2)
C9	H9A	0.980
C9	H9AB	0.980
C9	H9AC	0.980
C10	C11	1.493(2)
C11	C12	1.402(2)
C11	C16	1.385(2)
C12	H12	0.950
C12	C13	1.388(2)
C13	C14	1.402(2)
C14	H14	0.950
C14	C15	1.388(2)
C15	C16	1.400(2)
C16	H16	0.950
C17	H17A	0.980
C17	H17B	0.980
C17	H17C	0.980
C18	H18A	0.980
C18	H18B	0.980
C18	H18C	0.980
C19	C20	1.493(2)
C19	C21	1.498(2)
C20	H20A	0.980
C20	H20B	0.980
C20	H20C	0.980
C21	H21A	0.980
C21	H21B	0.980
C21	H21C	0.980
C22	C23	1.503(4)
C22	C24	1.473(3)
C22	O10	1.255(4)
C23	H23A	0.980
C23	H23B	0.980
C23	H23C	0.980
C24	H24A	0.980
C24	H24B	0.980

C24	H24C	0.980

$Ru_2(OBz\text{-}F)_4(Me_2CO)_2$

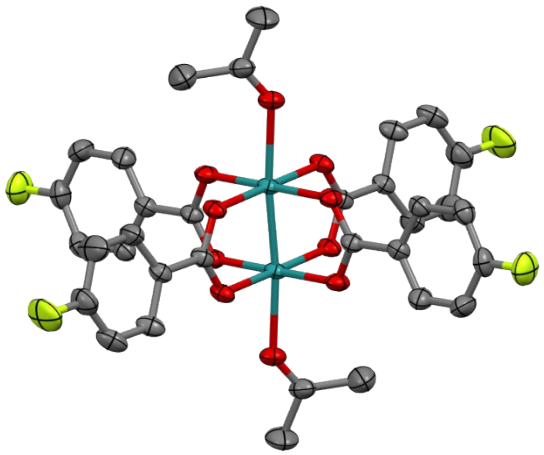

Figure S 8: ORTEP representation of $Ru_2(OBz\text{-}F)_4(Me_2CO)_2$ with 50% probability level.

Table S 5: SC-XRD data of the complex $Ru_2(OBz\text{-}F)_4(Me_2CO)_2$.

Compound	**$Ru_2(OBz\text{-}F)_4(Me_2CO)_2$**
Formula	$C_{34}H_{28}F_4O_{10}Ru_2$
CCDC	2043846
Formula weight	874.70
Temperature (K)	100(2)
Wavelength (Å)	0.7103 (Mo-K_α)
Crystal system	monoclinic
Space group	C 1 2/c 1
Z	8
a (Å)	29.179(10)
b (Å)	18.400(7)
c (Å)	17.212(6)
α (°)	90
β (°)	113.270(11)
γ (°)	90
Volume (Å^3)	8489.0(5)
μ (mm^{-1})	0.775

d_{calc} (g/cm^3)	1.639
F (000)	3488
Crystal size (mm^3)	0.049 x 0.185 x 0.345
Theta range	2.21° to 25.35°
Index range	-35 ≤ h ≤ 35
	-22 ≤ k ≤ 22
	-20 ≤ l ≤ 20
Refl. collected	131612
Independent reflections	7767 (R_{int} = 0.0553)
Data/restraints/parameters	7767 / 0 / 422
GOF on F^2	1.139
R_1/wR_2[a]	0.0773 / 0.2202
[I ≥ 2σ(I)][b]	
R_1/wR_2	0.0843 / 0.2320
[all data]	
Largest diff. peak and hole	2.592 and -2.341 eÅ^{-3}

a: $w = 1/\left[\sigma^2\left(F_o^2\right) + (0.1582P)^2 + 57.6731P\right]$ where $P = (F_o^2 + 2F_c^2)/3$

b: $R_1 = \sum \| F_o| - |F_c \| / \sum |F_o|$; $wR_2 = \{\sum [w\left(F_o^2 - F_c^2\right)^2] / \sum [w(F_o^2)^2]\}^{1/2}$

Atom1	Atom2	Length
Ru1	O1	2.070(4)
Ru1	O3	2.074(5)
Ru1	O10	2.346(6)
F1	C5	1.361(8)
F2	C12	1.38(1)
O1	C1	1.269(7)
O2	C1	1.279(8)
O3	C8	1.276(9)
O4	C8	1.266(8)
O10	C32	1.216(9)
C1	C2	1.477(7)
C2	C3	1.388(9)
C2	C7	1.40(1)
C3	C4	1.37(1)
C3	H3	0.950
C4	C5	1.39(1)
C4	H4	0.950

C5	C6	1.37(1)
C6	C7	1.381(9)
C6	H6	0.949
C7	H7	0.950
C8	C9	1.48(1)
C9	C10	1.39(2)
C9	C14	1.38(2)
C10	C11	1.40(2)
C10	H10	0.95
C11	C12	1.34(1)
C11	H11	0.95
C12	C13	1.40(2)
C13	C14	1.38(2)
C13	H13	0.95
C14	H14	0.95
C32	C33	1.50(1)
C32	C34	1.51(1)
C33	H33A	0.980
C33	H33B	0.982
C33	H33C	0.978
C34	H34A	0.98
C34	H34B	0.98
C34	H34C	0.981
Ru02	O5	2.069(4)
Ru02	O7	2.076(6)
Ru02	O9	2.316(4)
F3	C19	1.371(9)
F4	C26	1.36(1)
O5	C15	1.264(7)
O6	C15	1.265(6)
O7	C22	1.279(8)
O8	C22	1.262(7)
O9	C29	1.212(8)
C15	C16	1.497(8)
C16	C17	1.37(1)
C16	C21	1.410(9)
C17	C18	1.40(1)
C17	H17	0.950
C18	C19	1.38(1)
C18	H18	0.949
C19	C20	1.36(1)
C20	C21	1.370(9)
C20	H20	0.949
C21	H21	0.949
C22	C23	1.49(1)
C23	C24	1.391(9)
C23	C28	1.37(1)
C24	C25	1.40(1)
C24	H24	0.950

C25	C26	1.38(1)
C25	H25	0.950
C26	C27	1.37(1)
C27	C28	1.40(1)
C27	H27	0.951
C28	H28	0.951
C29	C30	1.53(1)
C29	C31	1.48(1)
C30	H30A	0.98
C30	H30B	0.98
C30	H30C	0.98
C31	H31A	0.98
C31	H31B	0.98
C31	H31C	0.98

Structural Properties of Diruthenium Tetracarboxylates – Bond Lengths and Angles

*Table S 6: Overview on selected bond lengths and angles found in diruthenium tetracarboxylates in literature and presented in this work. *Always the angle <90° was selected, **Average value (there are two Ru atoms in the asymmetric unit, belonging to two complexes).*

Equatorial carboxylate	Axial ligand	d_{Ru-Ru} [Å]	$d_{Ru-O(eq)}$ [Å]**	$d_{Ru-L(ax)}$ [Å]	$\omega_{O(eq)-Ru-O(eq)}$ [°]*	$\tau_{Oeq-Ru-Ru-Oeq}$ [°]	Ref.
Univalent $Ru^{II,II}$ PWs							
Acetate	H_2O	2.262	2.068	2.335	87.75	1.18	[2]
Acetate	MeOH	2.265	2.073	2.333	89.65	0.21	[5]
Trifluoroacetate	THF	2.277	2.074	2.268	87.69	0.16	[6]
Propionate	Acetone	2.2595	2.0675	1.363	89.74	0.40	[2]
Benzoate	Benzoic acid	2.2634	2.0535	2.356	89.65	0.53	[7]
Benzoate	Acetone	2.2608	2.0650	2.3467	98.66	3.92	[5]
Benzoate	THF	2.2667	2.0585	2.353	87.61	0.59	[8]
4-fluoro benzoate	Acetone	2.2698**	2.0698	2.3317**	89.31	0.55	This work
4-fluoro benzoate	THF	2.2677	2.061	2.354	89.80	0.85	[9]
3,5-difluoro benzoate	THF	2.2708	2.073	2.310	88.58	0.59	[9]
2,4,6-trifluoro benzoate	THF	2.2723	2.071	2.283	89.42	0.25	[9]
4-trifluoro-methyl benzoate	THF	2.2656	2.0610	2.3019	89.04	0.82	This work
4-trifluoro-methyl benzoate	THF (THF solvate)	2.2662	2.065	2.298	88.72	0.30	[10]
4-methoxy benzoate	Acetone	2.2687	2.0558	2.3415	89.29	0.24	This work
3,5-dimethoxy benzoate	Acetone	2.2679	2.0628	2.3342	89.43	0.49	This work
4-methyl benzoate	Acetone	2.2585	2.0550	2.3503	89.73	0.37	This work
Mixed-valence $Ru^{II,III}$ PWs							
Acetate	Chloride	2.2800	2.0229	2.5722	89.50	0.58	[11]
Acetate	Pyridine (PF_6^- anion)	2.2805	2.03	2.27	89.19	1.65	[12]
Acetate	4-methyl Pyridine (PF_6^- anion)	2.2786	2.019	2.291	88.76	0.43	[12]
Acetate	Quinuclidine (PF_6^- anion)	2.2918	2.025	2.338	88.72	0.83	[12]

Additional Information – Ligand Exchange Test Reaction

To systematically unveil ligand exchange properties of the obtained series of diruthenium tetrabenzoate derivatives, we conducted additional NMR-based ligand exchange reactions. Best mimicking the properties of BTC with electron withdrawing groups in meta position but being chemically inert, we selected 3,5-bis(trifluoromethyl) benzoic acid as competing ligand (coligand) for this test reaction. In Figure S 9, initial ligand exchange rates (black circles) and the found equilibrium constants (grey squares) are displayed as a function of the respective ligand pK_a. Details on procedure and data evaluation are provided in the ESI. Although not in a very strict order, a general trend towards lower exchange rates for more acidic precursor ligands can be extracted. It remains unclear why OBz-Me has a comparably low rate. Overall, exchange rates between 1 and 8 h^{-1} (at ambient temperature) confirm the slow ligand exchange kinetics for PGM-PW complexes. Equilibrium constants were extracted from the ratio of free precursor acid to the acid of the coligand after thermodynamic equilibration for 120 min at 55 °C. Entropic contribution is not to be expected for such a stoichiometric exchange reaction. A general correlation can be seen. Following chemical intuition, rather basic ligands are substituted preferentially as they tend to be protonated upon their dissociation and thus, are partially removed from the equilibrium.

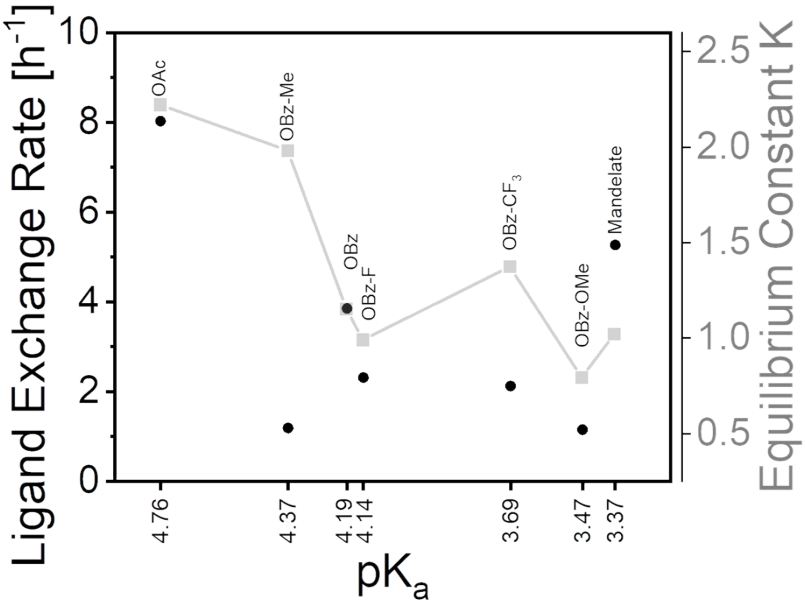

Figure S 9: Correlation between the ligand exchange rate (black circular data points), the equilibrium constant K (grey square data points) and the respective precursor ligand acidity (pK_a). The ligand exchange was performed with 3,5-bis(trifluoromethyl) benzoic acid as monofunctional BTC simulant. Ligand exchange rates were determined using the maximum initial slopes at ambient temperature. Equilibrium constants are determined using the ratio of released precursors ligand to free coligand (equimolar feed) upon equilibration at 55 °C.

Generally, the ligand exchange is controlled by the acidity of the respective carboxylic acids. Although more basic ligands form stronger bonds to the metal rendering them more difficult to dissociated, their basicity prevents them from reversible coordination as their protonation occurs upon release. On the contrary, more acidic ligands are preferentially deprotonated but might form relatively weak coordination bonds to the metal. Due to these competing effects, a final decision on the ideal MOF precursor on the basis of this NMR-based simulating experiment is not substantiated but requires the experimental MOF syntheses and careful analysis of the respective materials as outlined in the following. However, the the two samples OBz and mandelate seem to have higher ligand exchange rates compared to the other investigated benzoate ligands.

As follows, Figure S 10 shows an exemplary NMR spectrum how the calculation of kinetic and thermodynamic data was extracted from the primary data. Figure S 11 gives an impression on the

evolution of related NMR spectra throughout the experiment exemplified by $Ru_2(OBz)_4$. Figure S 12 summarizes the evolution of the ratio of free precursor ligand to coligand for the whole series of diruthenium benzoate precursors.

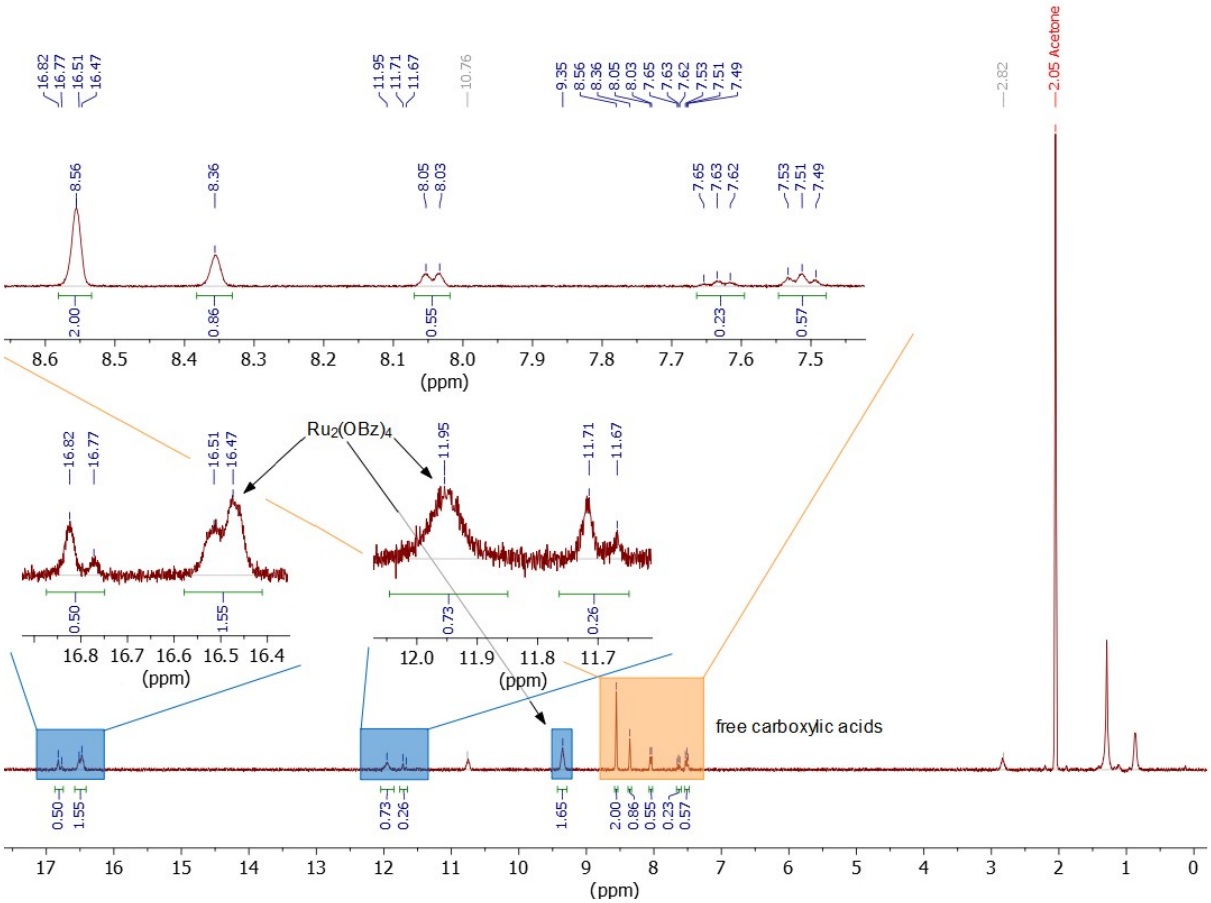

Figure S 10: Exemplary ^{1}H-NMR spectrum of the ligand exchange reaction with $Ru_2(OBz)_4$ and 3,5-bis(trifluoromethyl) benzoic acid as competitive coligand after 6min 27s at ambient temperature. The signals of ligands bound to complexes are highlighted with blue, the region of free acids is highlighted in orange. Equilibrium konstants were determined using the ratios of the free acids as paramagnetism of the diruthenium core obstructs quantification of bound ligands.

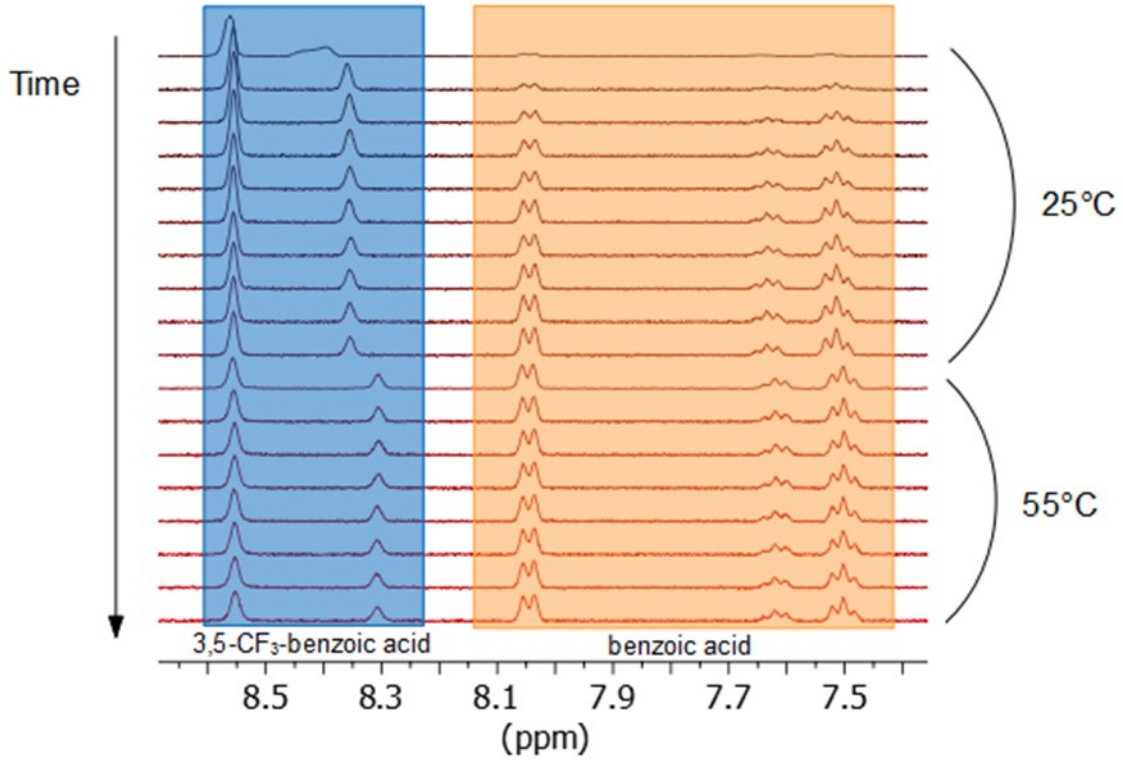

Figure S 11: Stacked ^{1}H-NMR spectra of the kinetic series recorded for $Ru_2(OBz)_4$ as example.

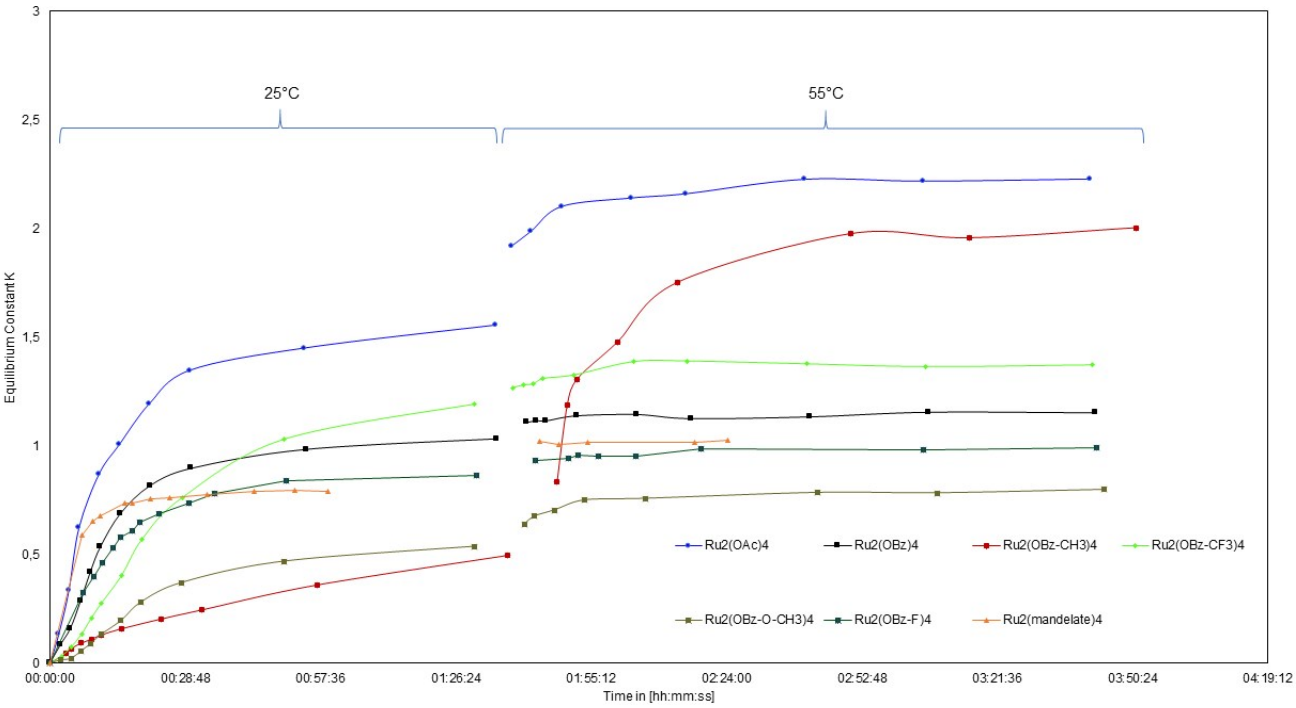

Figure S 12: Evolution of the ligand exchange reaction between precursor complexes and 3,5-bis(trifluoromethyl) benzoic acid as monotopic BTC simulant. The graphs display the ratio of the released precursor ligand to free coligand as a function of time. The gap at 1:30 h between the curves represents the transition from r.t. to 55 °C. Horizontal plateaus of the curves indicate reached equilibria. The steepest slopes in the beginning of the reactions were taken to calculate the exchange rates.

Additional Information – MOF Characterization

Development of a Modified MOF Synthesis Procedure

On the basis of the established Ru-HKUST-1 synthesis procedure utilizing $Ru_2(OAc)_4$ precursor and HOAc modulator, we developed a modified procedure to account for the different solubility of benzoate-derived precursors and benzoic acid derivatives as modulator. In contrast to the acetic acid, any solubilizing effect and function as cosolvent enhancing H_3BTC dissolution is absent for benzoic acids. Thus, we investigated the suitability of a water acetone mixture for MOF syntheses.

The following Table S 7 summarizes the outcome of MOF syntheses dedicated to extract the ideal synthetic procedure for this study. In each reaction, 158 mg $Ru_2(OAc)_4$ precursor and 101 mg H_3BTC were dissolved in the stated solvent / modulator mixture and heated to 150 °C over 3 d. Test reactions A, B and C yielded crystalline powders featuring the HKUST-1 structure, while reaction D resulted in an amorphous gel. Respective PXRD patterns are provided in Figure S 13. To avoid gel formation and to minimize the modulator loading, we selected the conditions of test reaction C for the study. For reasons of comprehensiveness, test reaction B was included in the results section of the main manuscript denoted as "OAc (x2 Mod)".

*Table S 7: Solvent amounts used to extract the ideal MOF synthesis conditions for this study. For each reaction, 158 mg $Ru_2(OAc)_4$ precursor and 101 mg H_3BTC were dissolved in the stated solvent / modulator mixture and heated to 150 °C for 3 d. *related PXRD patterns are displayed in Figure S 13 below.*

Test reaction	H_2O [mL]	Me_2CO [mL]	HOAc [mL]	Outcome
A	2	2	0.7	Crystalline powder*
B	4	4	1.4	Crystalline powder*
C	4	4	0.7	Crystalline powder*
D	4	4	0.3	Amorphous gel

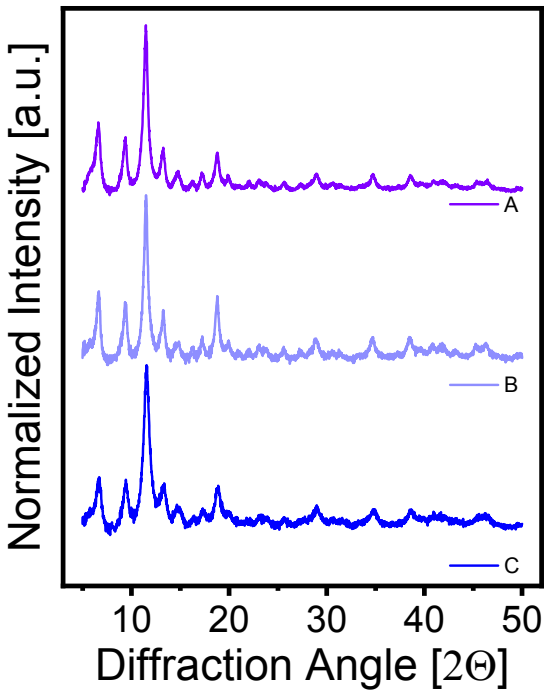

Figure S 13: Comparison of PXRD patterns for the MOF synthesis optimisation following test reactions A, B and C. All three patterns indicate crystalline and phase pure MOF materials.

MOF Synthesis Details

Table S 8: Used reagent amounts for the synthesis of Ru-HKUST-1 samples. All syntheses using 4 mL water and 4 mL acetone were performed under inert conditions in steel autoclaves with Teflon liners at 150 °C over 3 days.

MOF sample	Precursor (Ru_2R_4)			Linker H_3BTC			Modulator		
	Molar weight [$gmol^{-1}$]	Mass [mg]	Eq	Molar weight [$gmol^{-1}$]	Mass [mg]	Eq	Species	Mass [mg]	Eq
OAc	438.32	158.0	3	210.14	101	4	HOAc	735	102
OAc (x2mod)	438.32	158.0	3	210.14	101	4	HOAc	1470	204
OBz	686.60	247.5	3	210.14	101	4	HOBz	1490	102
OBz-F	758.56	273.1	3	210.14	101	4	HOBz-F	1710	102
OBz-CF_3	958.59	345.1	3	210.14	101	4	HOBz-CF_3	2320	102
OBz-Me	742.71	267.4	3	210.14	101	4	HOBz-Me	1660	102
OBz-OMe	806.70	290.4	3	210.14	101	4	HOBz-OMe	1860	102
L-mandelate	806.70	290.4	3	210.14	101	4	L-mandelic acid	1860	102

Sample Appearance

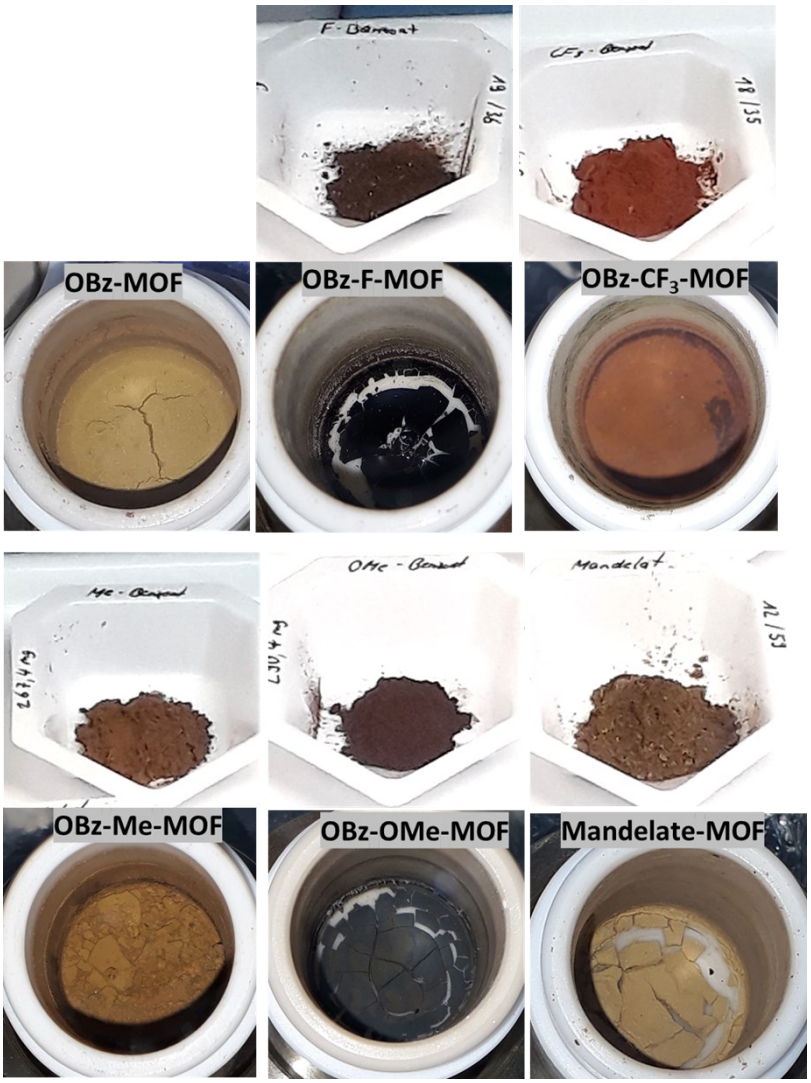

Figure S 14: Similarity of color shade between precursor complex and derived activated MOF.

Powder X-Ray Diffraction

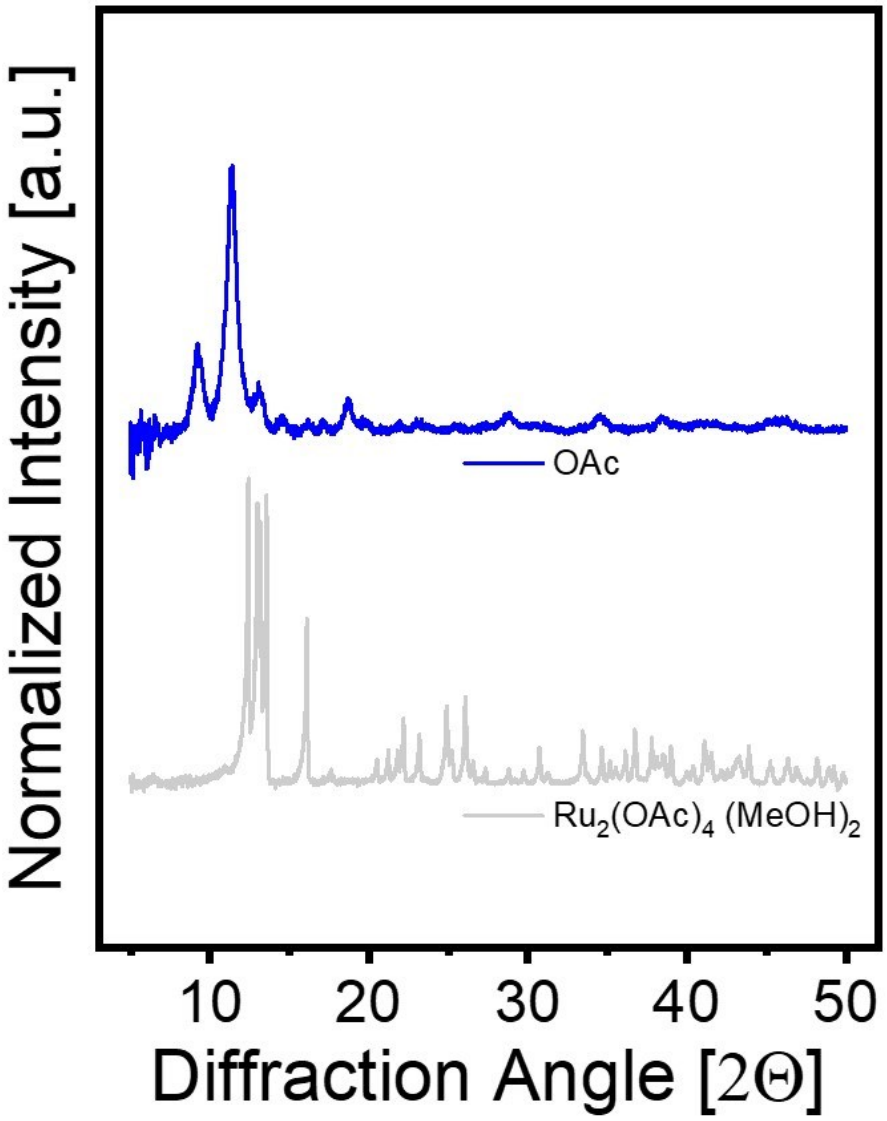

Figure S 15: PXRD comparison of Ru-HKUST-1 (top trace, blue) with its acetate precursor (bottom trace, light grey). Note that the crystalline precursor adduct was desolvated prior to use in MOF syntheses.

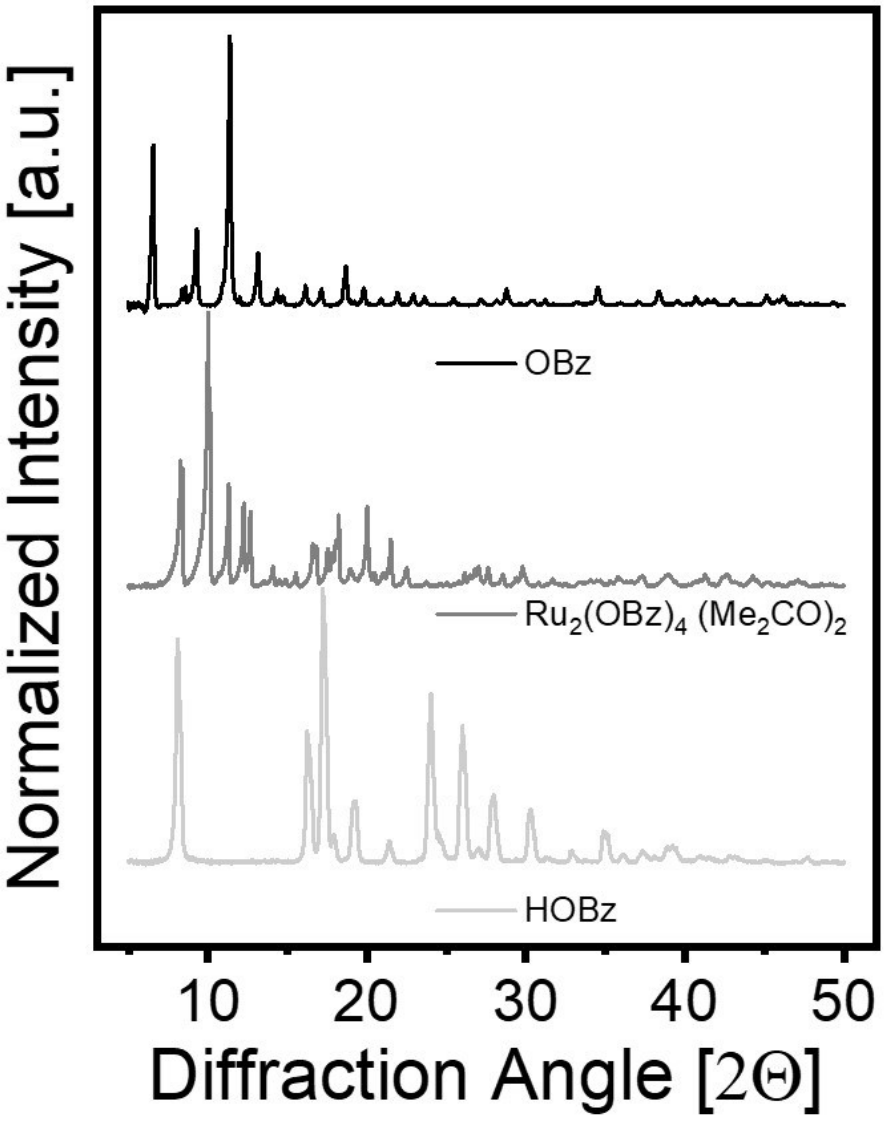

Figure S 16: PXRD comparison of Ru-HKUST-1 (top trace, black) with its benzoate precursor (middle trace, dark grey) and the used free acid modulator (bottom trace, light grey). Note that the crystalline precursor adduct was desolvated prior to use in MOF syntheses.

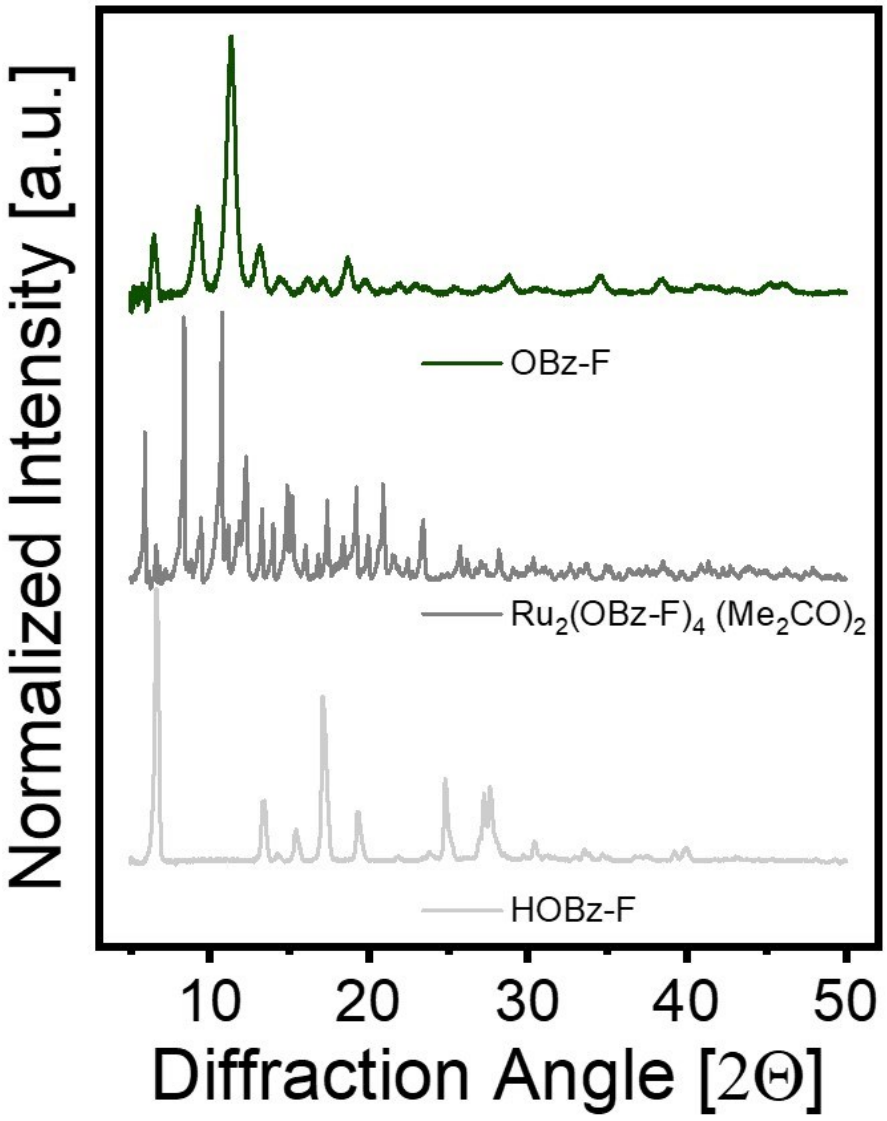

Figure S 17: PXRD comparison of Ru-HKUST-1 (top trace, emerald) with its 4-fluoro benzoate precursor (middle trace, dark grey) and the used free acid modulator (bottom trace, light grey). Note that the crystalline precursor adduct was desolvated prior to use in MOF syntheses.

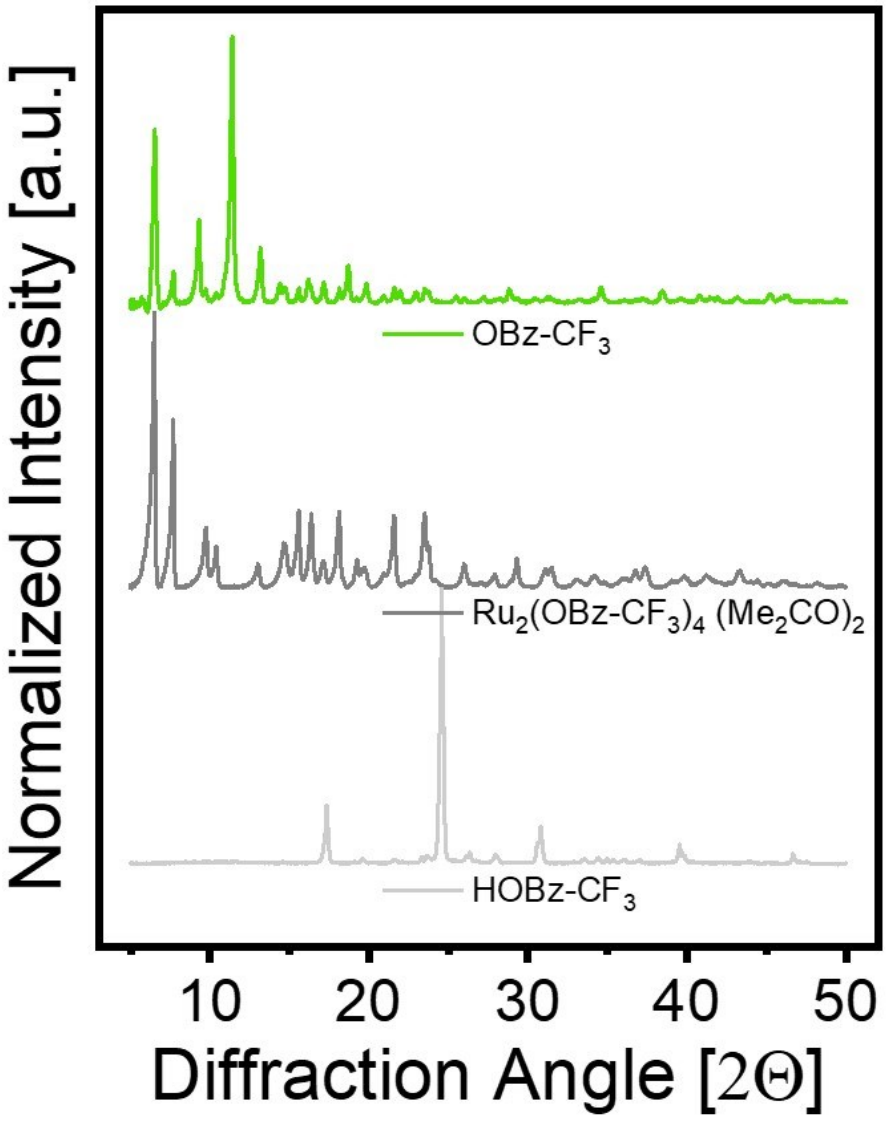

Figure S 18: PXRD comparison of Ru-HKUST-1 (top trace, green) with its 4-trifluoromethyl benzoate precursor (middle trace, dark grey) and the used free acid modulator (bottom trace, light grey). Note that the crystalline precursor adduct was desolvated prior to use in MOF syntheses.

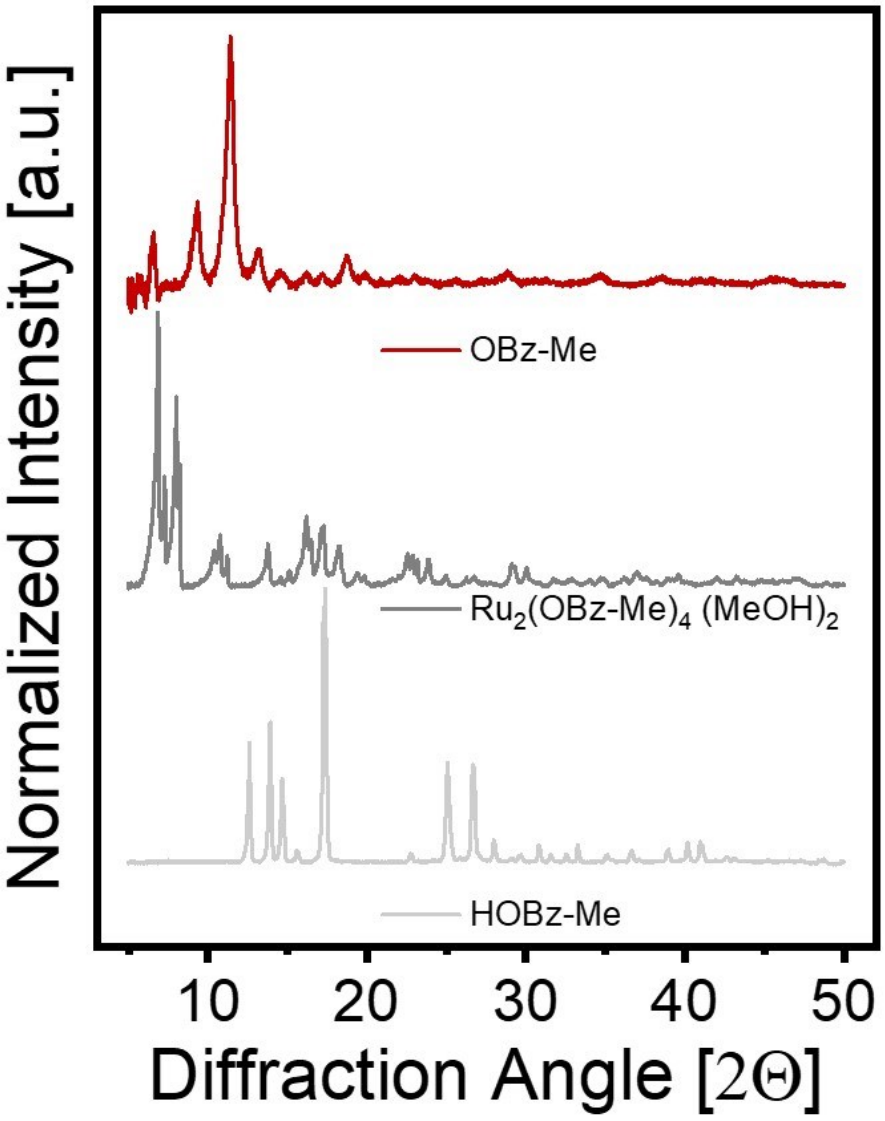

Figure S 19: PXRD comparison of Ru-HKUST-1 (top trace, red) with its 4-methyl benzoate precursor (middle trace, dark grey) and the used free acid modulator (bottom trace, light grey). Note that the crystalline precursor adduct was desolvated prior to use in MOF syntheses.

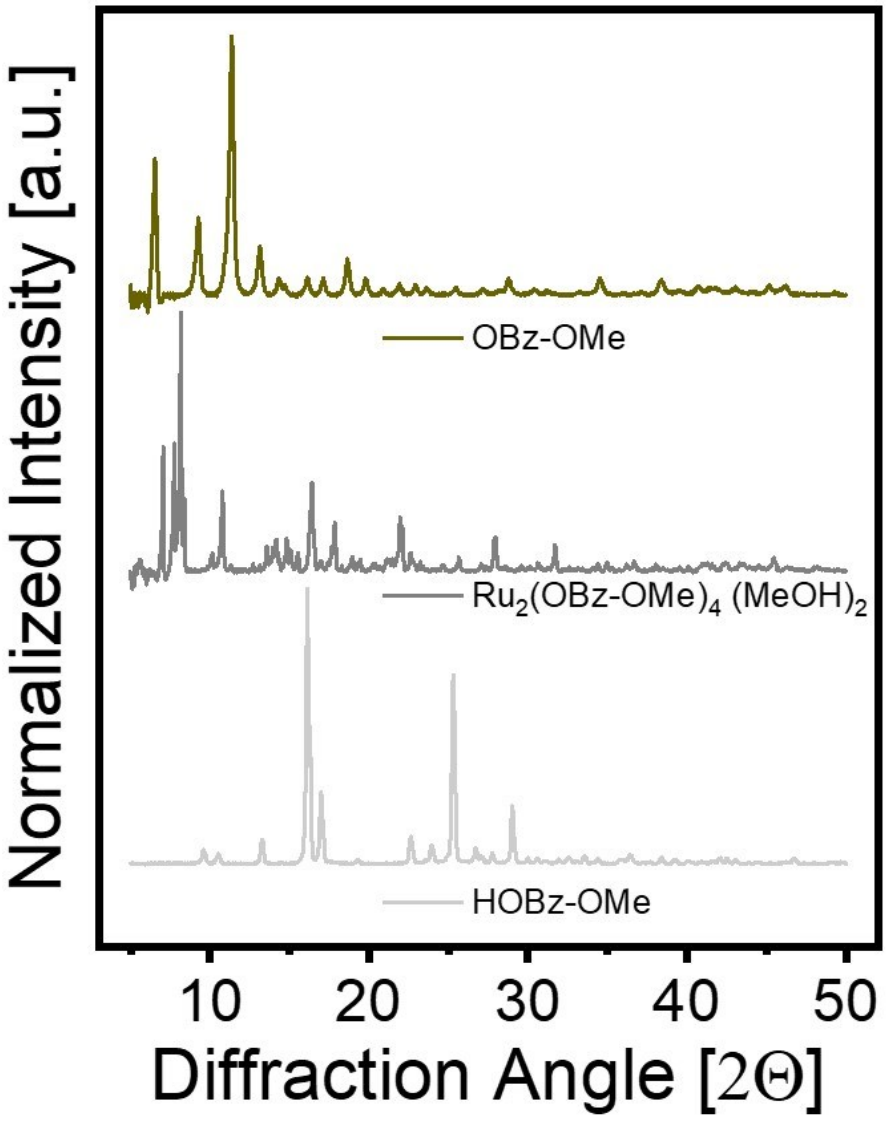

Figure S 20: PXRD comparison of Ru-HKUST-1 (top trace, olive) with its 4-methoxy benzoate precursor (middle trace, dark grey) and the used free acid modulator (bottom trace, light grey). Note that the crystalline precursor adduct was desolvated prior to use in MOF syntheses.

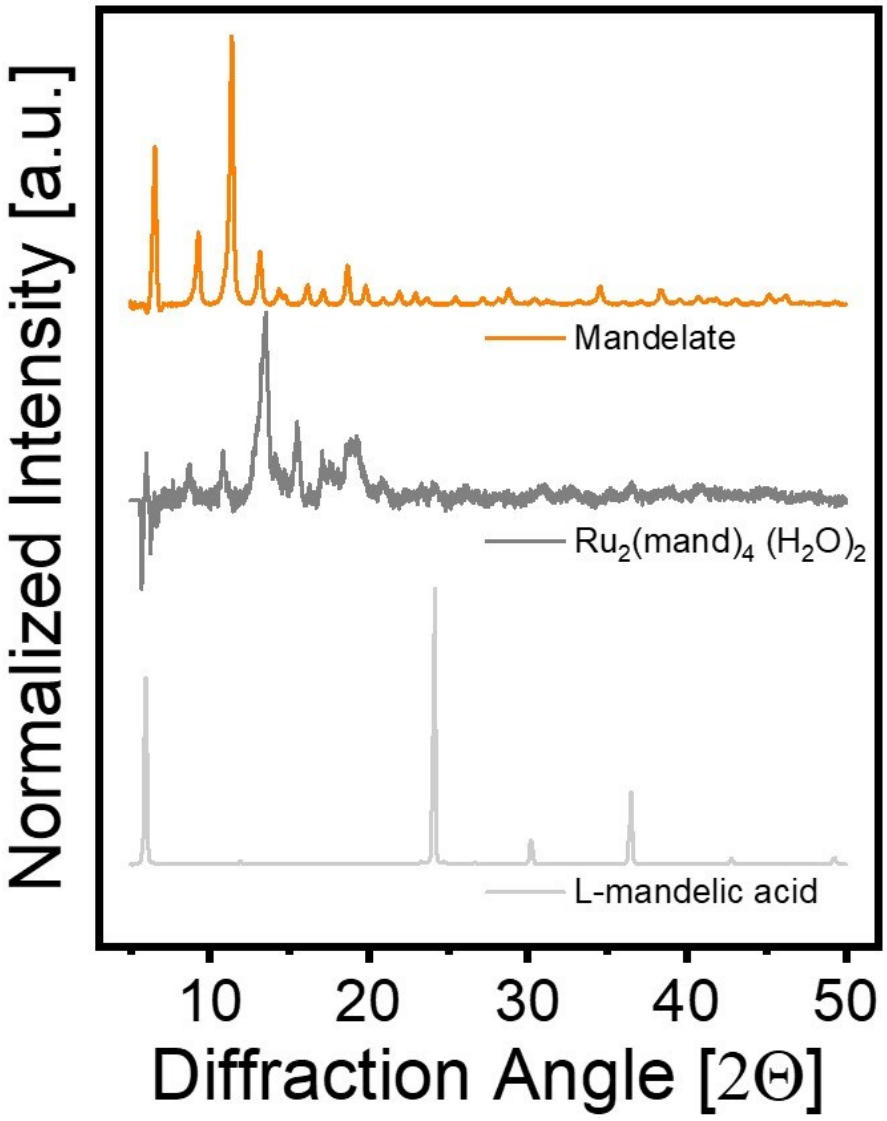

Figure S 21: PXRD comparison of Ru-HKUST-1 (top trace, orange) with its L-mandelate precursor (middle trace, dark grey) and the used free acid modulator (bottom trace, light grey). Note that the crystalline precursor adduct was desolvated prior to use in MOF syntheses.

Composition & Porosity

C and H elemental analysis was combined with Ru contents derived from TGA-based metal oxide residues and Ru:F ratios obtained from EDS analysis. The residual unknown elemental content is assigned to oxygen assumed as the only missing elemental component. A summary of all elemental contents together with the theoretical values of an ideal $[Ru_3(BTC)_2]$ structure is shown in Table S 9. Solver-derived sum formulae putatively describing the found experimental values are provided with several assumptions: Neither oxides, nor hydroxides, nor fluorides were considered as additional counterions. All calculations were limited to BTC^{3-}, $RCOO^-$ and H^+ with R being characteristic for each modulator/precursor ligand. No localisation of calculated protons to any counterions is possible from the obtained data, thus H^+ are involved in the sum formulae independently. Note, that the sum of organic charges (involving BTC^{3-}, $RCOO^-$ and H^+) was set to be ≥-6. This condition is based on the assumed $Ru^{II,II}$ sites and potential presence of Ru^0-NPs in some samples. Each sum formula was set to three Ru atoms per repeating unit.

*Table S 9: Summary of compositions of all samples. The experimentally determined elemental C, H, F and Ru contents served for a solver-approach using Microsoft Excel to derive the stated putative sum formulae. However, fitting did not provide unambiguous results for all samples. *the fitting of this sample gave inconsistencies or bad fitting quality. Elemental contents close to the ideal composition are highlighted in green, those very different from the ideal value are highlighted in red. Note, that the H^+ content of each sample calculated by this method is highly sensitive to experimental fluctuations and should not be overinterpreted. Considerably lower anion amounts per sum formula found for the OBz-OMe sample is in line with pronounced Ru^0-NP formation.*

Sample	Elemental contents [%]					Putative sum formula	Molar weight of repeating unit
	C	H	F	O*	Ru		
OAc	30.48	1.33	- -	27.8	40.4	$[Ru_3(BTC)_{1.83}(OAc)_{0.49}H_{2.09}]$	713.27
OAc (modx2)	30.60	1.28	- -	27.0	41.2	$[Ru_3(BTC)_{1.77}(OAc)_{1.17}H_{0.48}]$*	739.37
OBz	31.40	1.26	- -	25.4	41.9	$[Ru_3(BTC)_{1.78}(OBz)_{0.41}H_{1.63}]$	723.18
OBz-F	30.70	1.19	0.46	25.8	41.8	$[Ru_3(BTC)_{1.91}(OBz\text{-}F)_{0.18}H_{2.13}]$*	725.99
OBz-CF_3	33.74	1.42	3.03	29.2	32.6	$[Ru_3(BTC)_{2.58}(OBz\text{-}CF_3)_{0.5}H_{3.35}]$*	935.51
OBz-Me	31.67	1.47	- -	37.71	29.2	$[Ru_3(BTC)_{3.58}(OBz\text{-}Me)_0H_{4.74}]$*	1184.61
OBz-OMe	25.94	0.98	- -	22.7	50.4	$[Ru_3(BTC)_{1.40}(OBz\text{-}OMe)_{0.05}H_{1.28}]$	602.02
Mandelate	30.67	1.22	- -	26.4	41.7	$[Ru_3(BTC)_{1.93}(mand)_{0.16}H_{1.94}]$	729.08
Ideal $[Ru_3(BTC)_2]$	30.13	0.84	- -	26.76	42.26	$[Ru_3(BTC)_2]$	713.27

On the basis of these idealized (bottom row) and putative sum formulae (all other lines), their respective molecular weight of the repeating unit was used to normalize the found BET surface areas. The following Table S 10 provides an overview on molar BET surface areas [m^2mmol^{-1}] and the molar pore volumes [cm^3mmol^{-1}] of all samples. For comparison values of the ideal Cu-HKUST-1 structure are supplemented.

Table S 10: Gravimetric BET surface areas (SA) and molar SAs [m^2mmol^{-1}] and pore volumes (PV) [cm^3mmol^{-1}] derived from idealized and calculated putative sum formulae. Total pore volumes refer to pores <387 Å. For comparison, the ideal Cu-HKUST-1 data is also provided. The ideal sum formula refers to 717.44 mg $mmol^{-1}$ for Ru and 604.87 mg $mmol^{-1}$ for Cu. The calculated sum formulae and respective molar weights are given in Table S 9 (right column). The values for the ideal Cu-HKUST-1 are derived from DFT simulations conducted in Ref.[13] The enormous coincidence of surface area and pore volume of the mandelate-based Ru-MOF sample is highlighted in comparison with the structural simulation (bottom row). Note, that both ideal and calculated sum formulae give very similar molar values supporting the general approach used herein.

Sample	Gravimetric		Based on ideal sum formula $[Ru_3(BTC)_2]$		Based on calculated sum formulae*	
	BET SA [m^2g^{-1}]	BET PV [cm^3g^{-1}]	SA [m^2mmol^{-1}]	PV [cm^3mmol^{-1}]	SA [m^2mmol^{-1}]	PV [cm^3mmol^{-1}]
OAc	1493	0.618	1071.13792	0.444	1065	0.441
OAc (modx2)	n.d.		n.d.	n.d.	n.d.	0.000
OBz	1432	0.584	1027	0.420	1036	0.423
OBz-F	1516	0.973	1088	0.701	1101	0.706
OBz-CF_3	987	0.413	708	0.298	923	0.386
OBz-Me	1401	0.516	1005	0.372	1660	0.611
OBz-OMe	1505	0.585	1080	0.423	906	0.352
Mandelate	1789	0.681	1284	0.493	1304	0.497
Ideal $[Cu_3(BTC)_2]$	2137	0.820	1293	0.496	1293	0.496

Vibrational spectroscopy

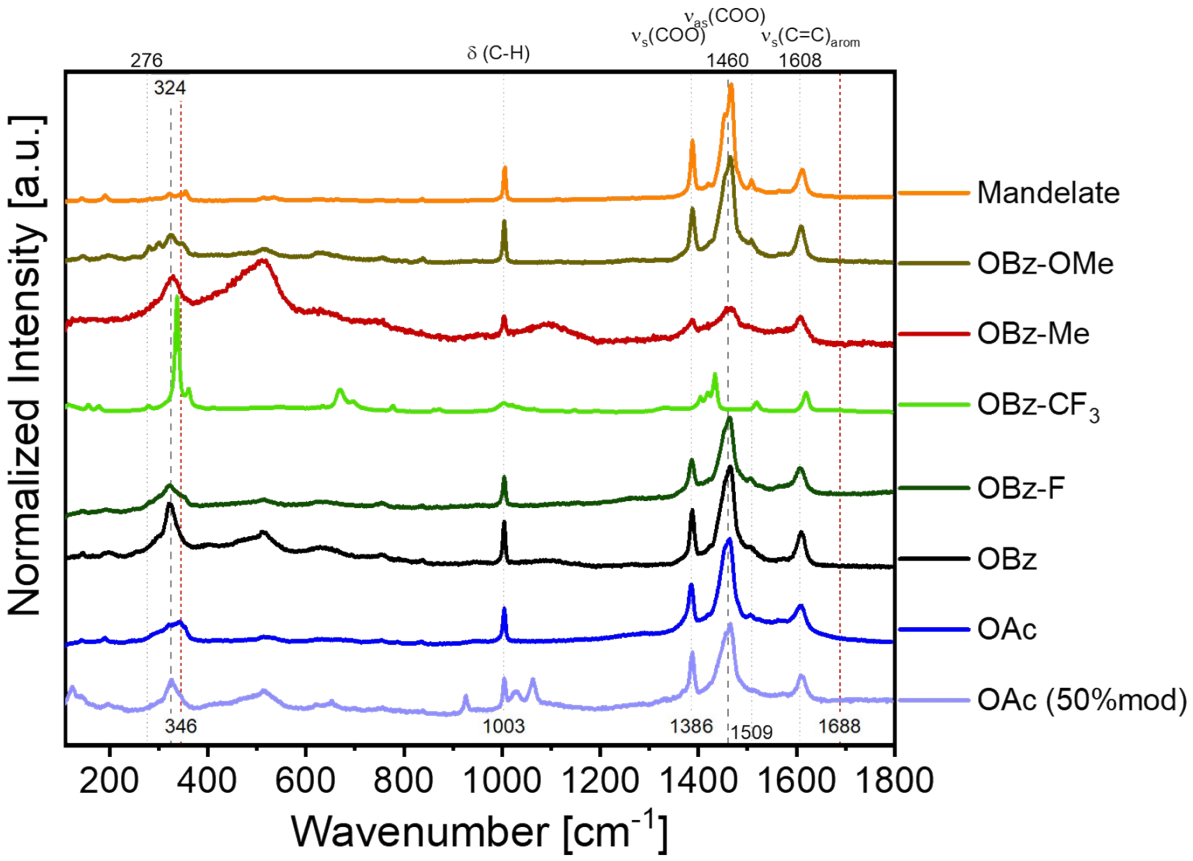

Figure S 22: Raman spectra of the whole Ru^{II,II}-HKUST-1 series indicate a generally identical bonding situation in all samples. However, the spectrum of OBz-CF$_3$ is dominated by strong signals arising from the respective modulator residues with the usually strong ν_{as}(COO) at 1460 cm^{-1} even not being visible. According to the absence of peaks around 1688 cm^{-1}, no free carboxylic acids are present in the samples.

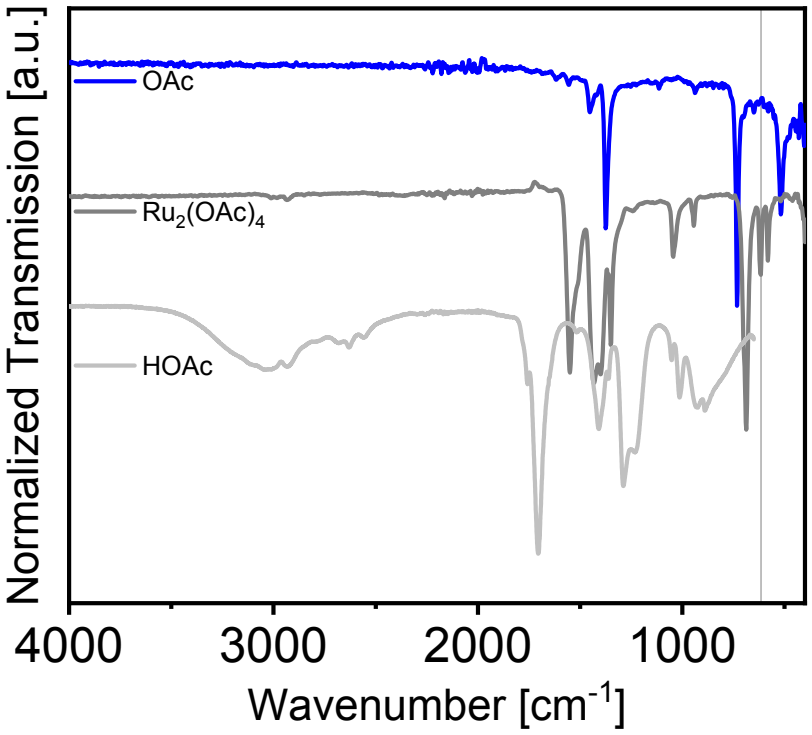

Figure S 23: Comparison of Ru-HKUST-1 (blue trace), the used OAc precursor (dark grey trace) and the free carboxylic acid (light grey trace). Vertical lines highlight vibration bands of the respective MOF sample which can not be assigned to the ideal MOF structure and thus, have to be associated with either precursor or modulator.

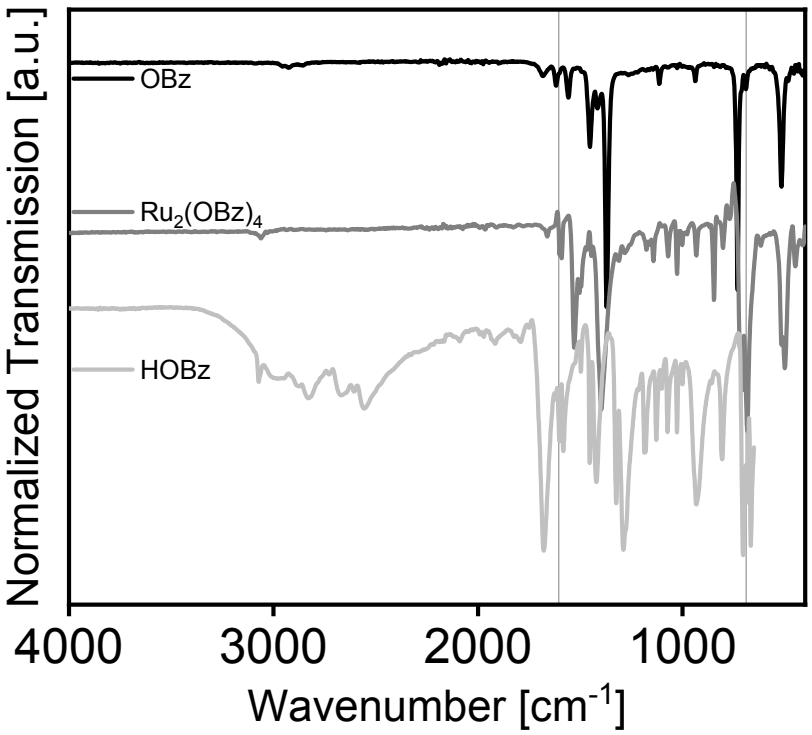

Figure S 24: Comparison of Ru-HKUST-1 (black trace), the used OBz precursor (dark grey trace) and the free carboxylic acid (light grey trace). Vertical lines highlight vibration bands of the respective MOF sample which can not be assigned to the ideal MOF structure and thus, have to be associated with either precursor or modulator.

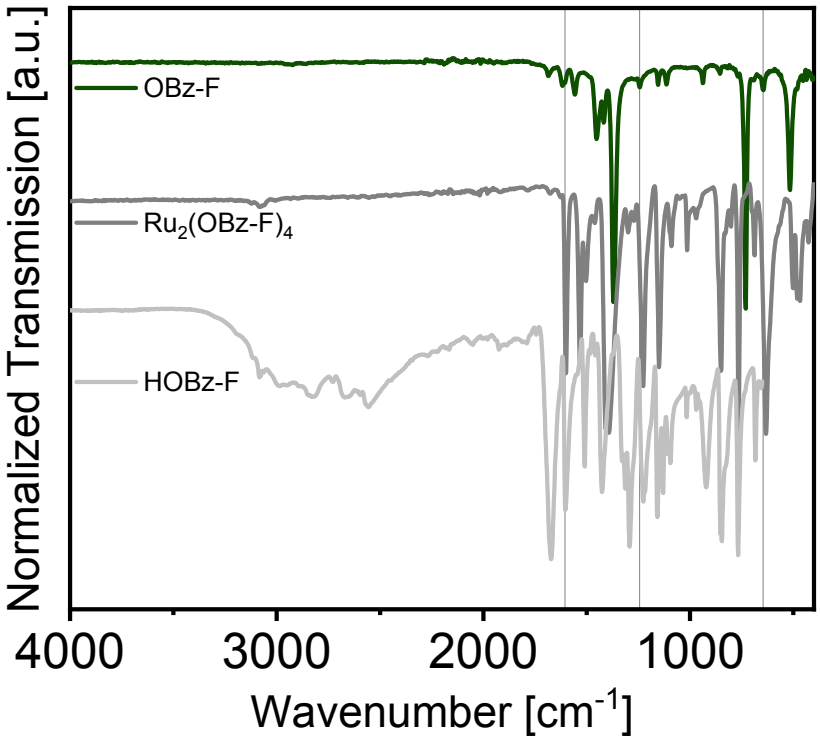

Figure S 25: Comparison of Ru-HKUST-1 (dark green trace), the used OBz-F precursor (dark grey trace) and the free carboxylic acid (light grey trace). Vertical lines highlight vibration bands of the respective MOF sample which can not be assigned to the ideal MOF structure and thus, have to be associated with either precursor or modulator.

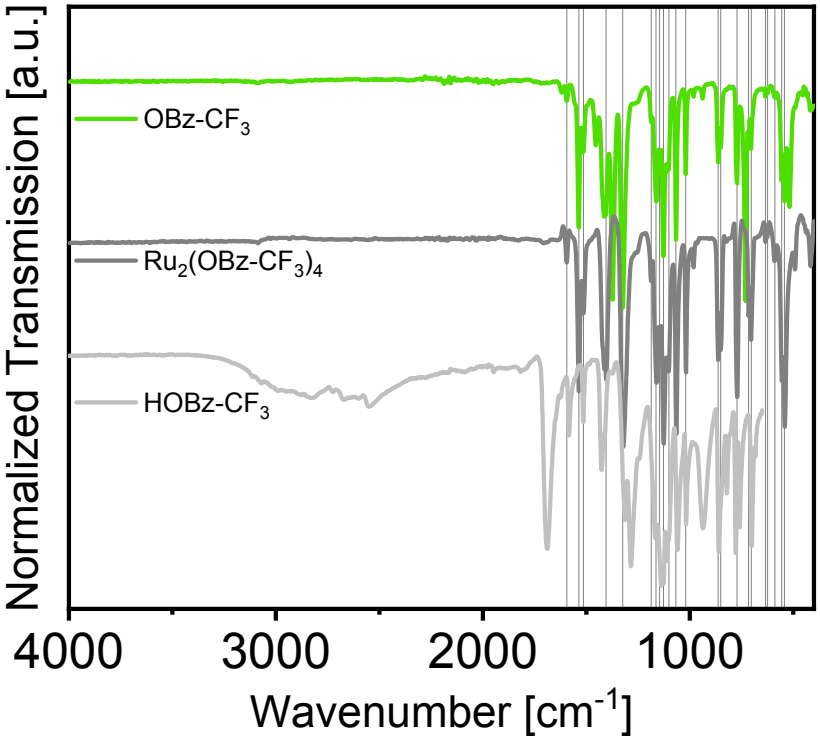

Figure S 26: Comparison of Ru-HKUST-1 (green trace), the used OBz-CF_3 precursor (dark grey trace) and the free carboxylic acid (light grey trace). Vertical lines highlight vibration bands of the respective MOF sample which can not be assigned to the ideal MOF structure and thus, have to be associated with either precursor or modulator. As compared to other samples of this series, the OBz-CF_3 spectra contain large amounts of residual precursor/modulator.

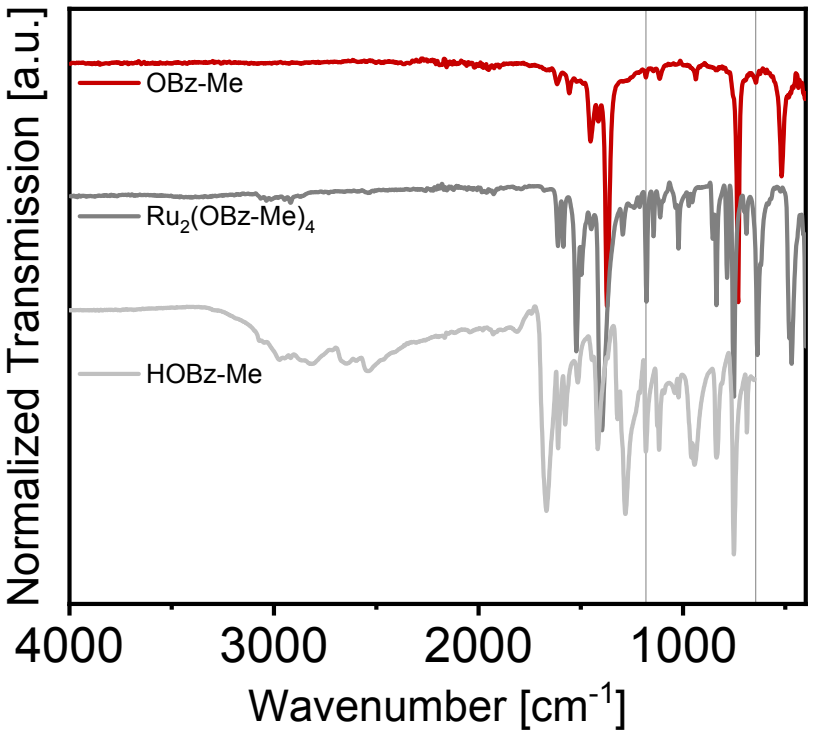

Figure S 27: Comparison of Ru-HKUST-1 (red trace), the used OBz-CF_3 precursor (dark grey trace) and the free carboxylic acid (light grey trace). Vertical lines highlight vibration bands of the respective MOF sample which can not be assigned to the ideal MOF structure and thus, have to be associated with either precursor or modulator.

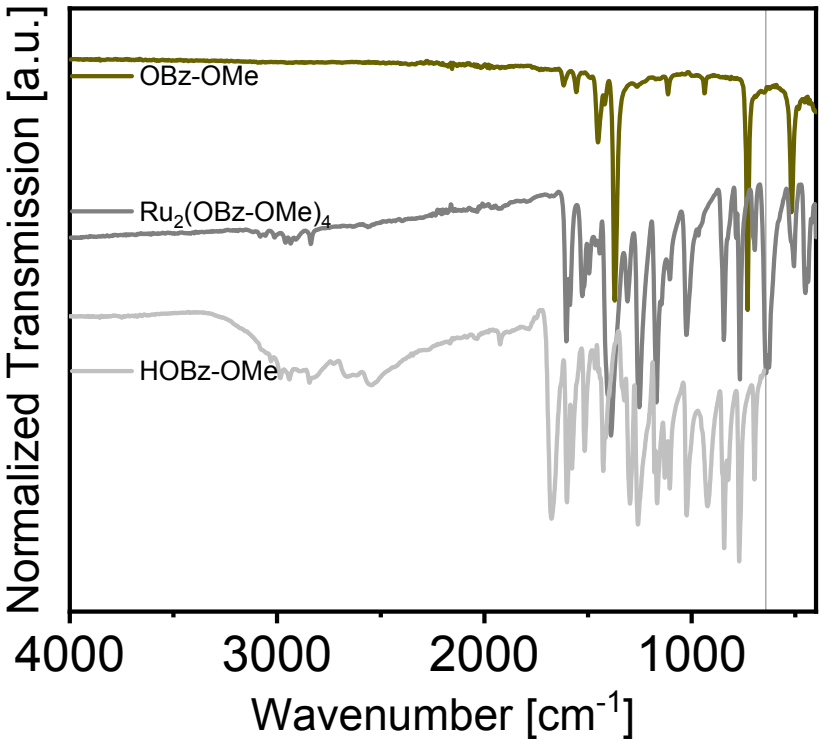

Figure S 28: Comparison of Ru-HKUST-1 (olive trace), the used OBz-CF_3 precursor (dark grey trace) and the free carboxylic acid (light grey trace). Vertical lines highlight vibration bands of the respective MOF sample which can not be assigned to the ideal MOF structure and thus, have to be associated with either precursor or modulator.

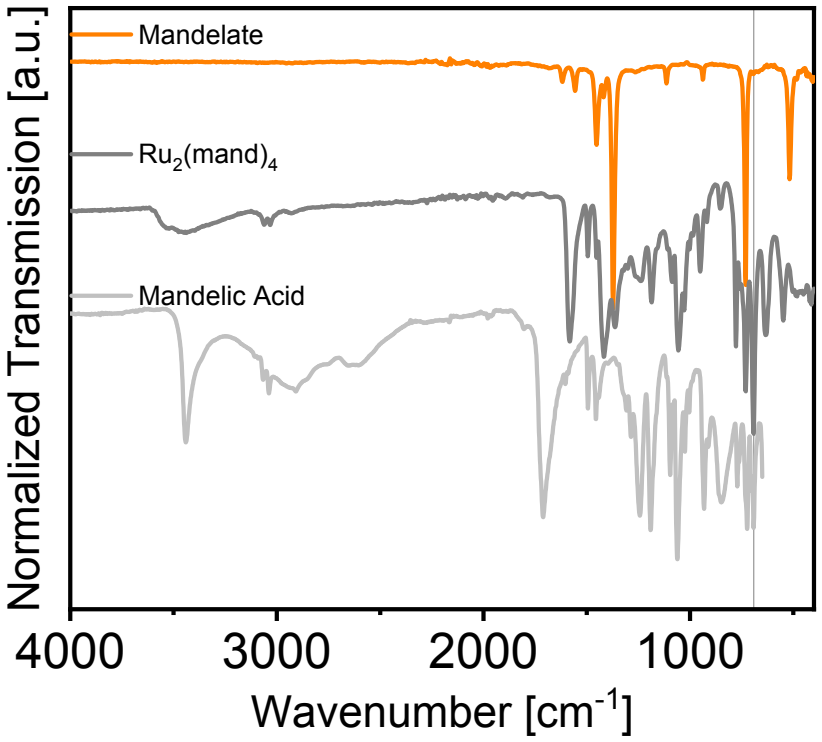

Figure S 29: Comparison of Ru-HKUST-1 (orange trace), the used OBz-CF_3 precursor (dark grey trace) and the free carboxylic acid (light grey trace). Vertical lines highlight vibration bands of the respective MOF sample which can not be assigned to the ideal MOF structure and thus, have to be associated with either precursor or modulator.

HR-TEM

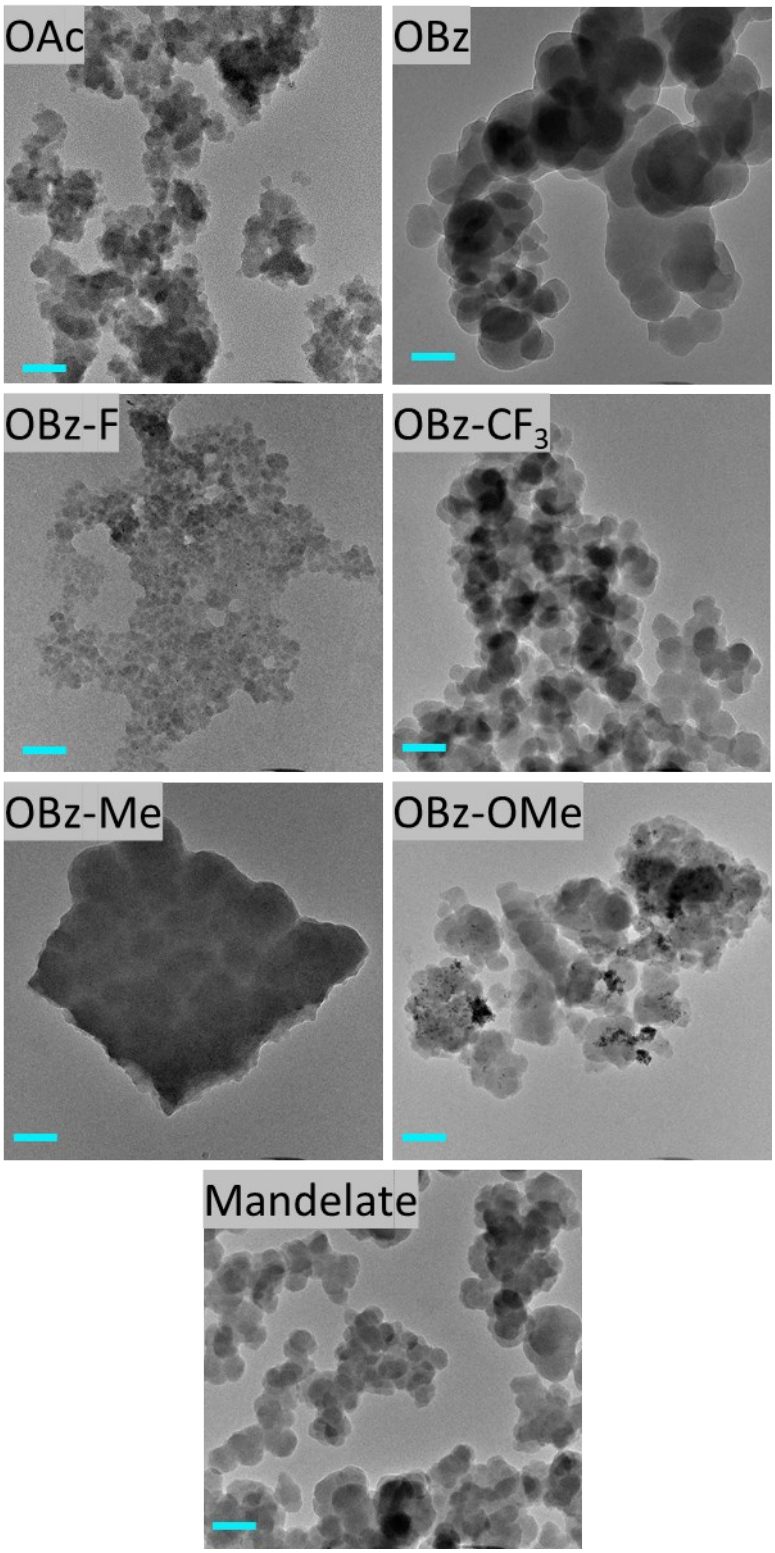

Figure S 30: HR-TEM images of all Ru-MOF samples. Blue scale bars represent 100 nm. The increased primary particle size particularly of the samples OBz, OBz-CF_3, OBz-Me and Mandelate is in line with results from FWHM analysis from PXRD patterns. The OAc and OBz-F samples contain few metal NPs while the OBz-OMe sample comprises higher amounts.

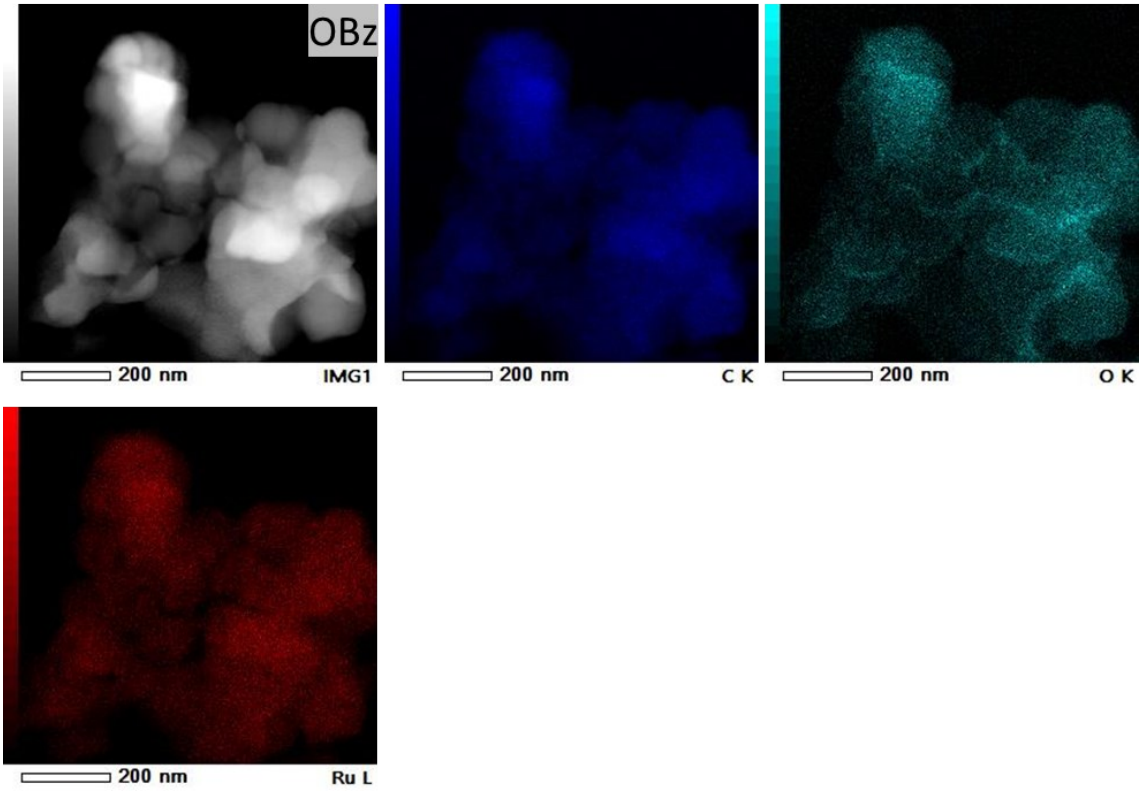

Figure S 31: A dark field STEM image of a representative particles of the OBz sample and corresponding EDS compositional maps of C, O and Ru indicates a homogeneous elemental distribution. Scale bars represent 200 nm.

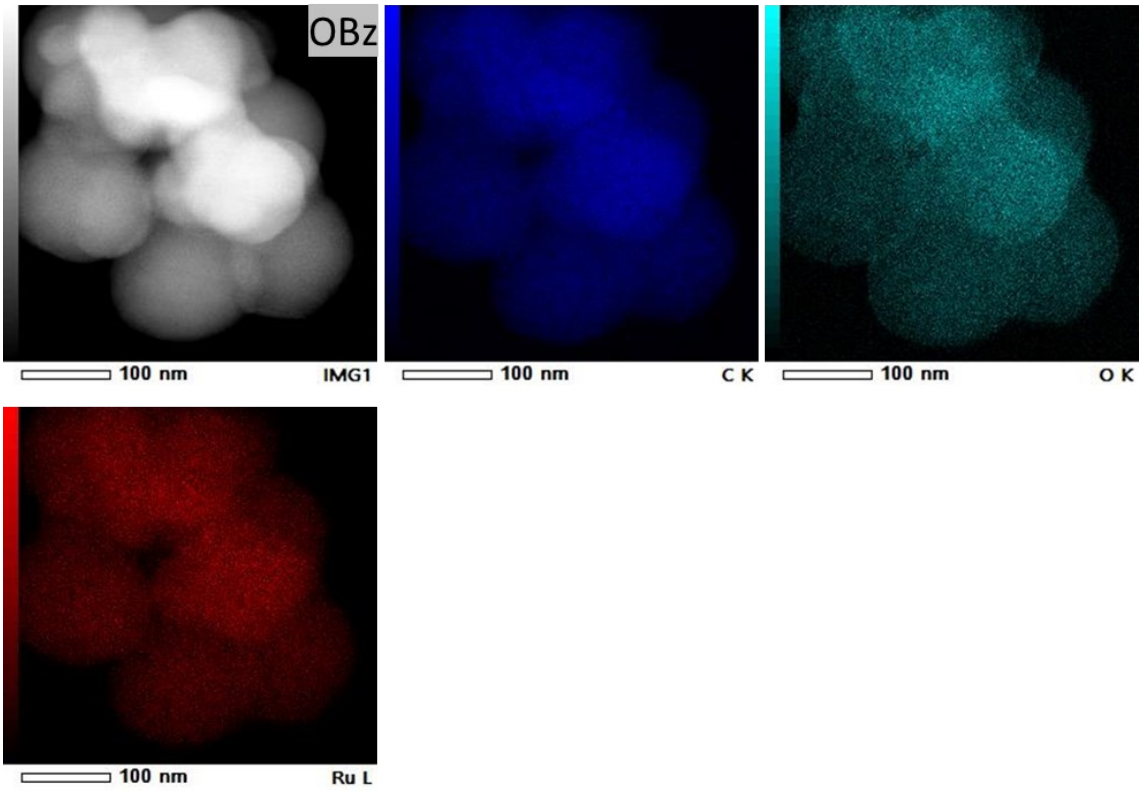

Figure S 32: A dark field STEM image of a representative particles of the OBz sample and corresponding EDS compositional maps of C, O and Ru indicates a homogeneous elemental distribution. Scale bars represent 100 nm.

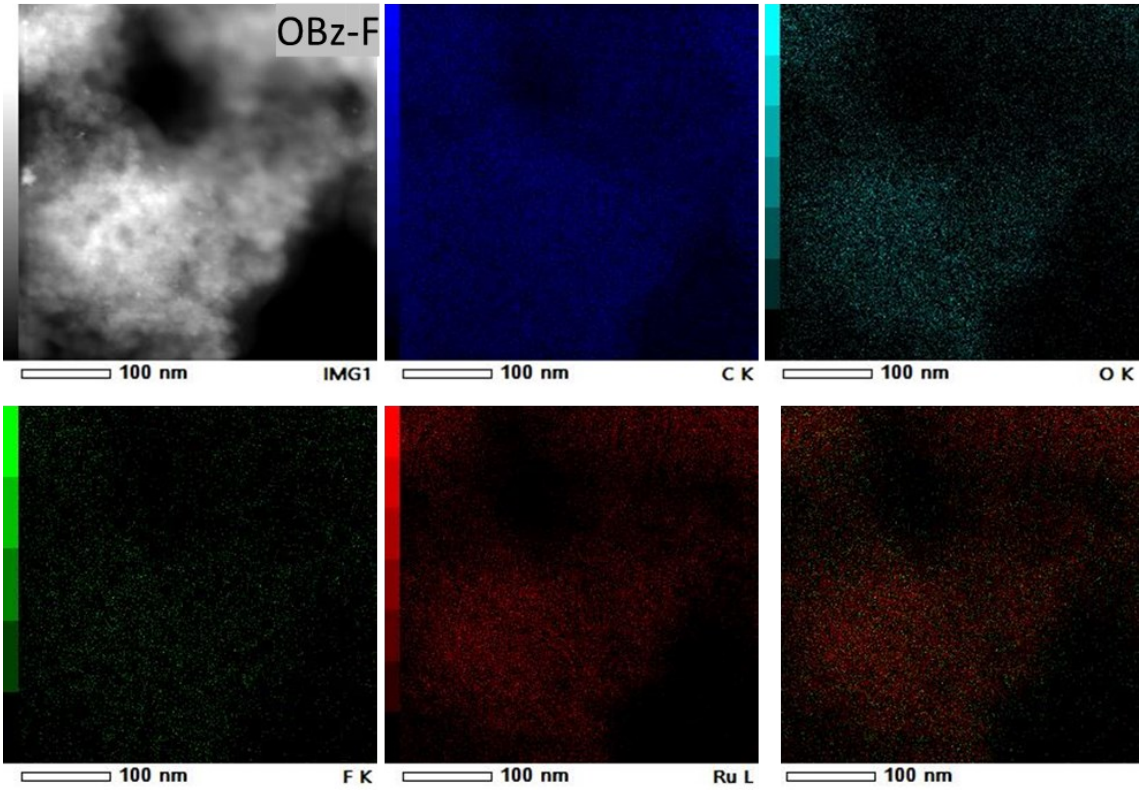

Figure S 33: A dark field STEM image of a representative particles of the OBz-F sample and corresponding EDS compositional maps of C, O and Ru indicates relatively homogeneous elemental distribution. Scale bars represent 100 nm. The bottom right image is an overlay of fluorine (green) and ruthenium (red). Due to the small particle size, clear conclusions on elemental inhomogeneities are difficult to draw.

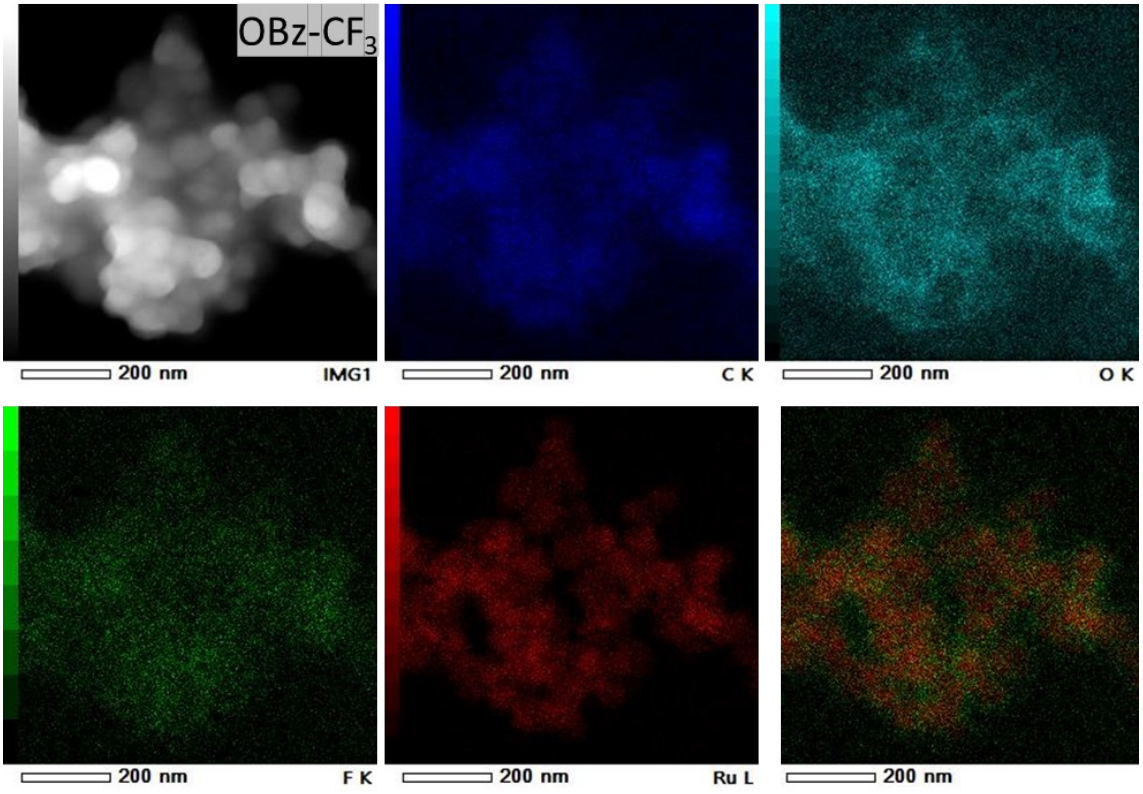

Figure S 34: A dark field STEM image of a representative particles of the OBz-CF_3 sample and corresponding EDS compositional maps of C, O, F and Ru and an overlay of F/Ru. Scale bars represent 200 nm. The bottom right image is an overlay of fluorine (green) and ruthenium (red). The images suggest the modulator to be preferentially located at the surface of the particles.

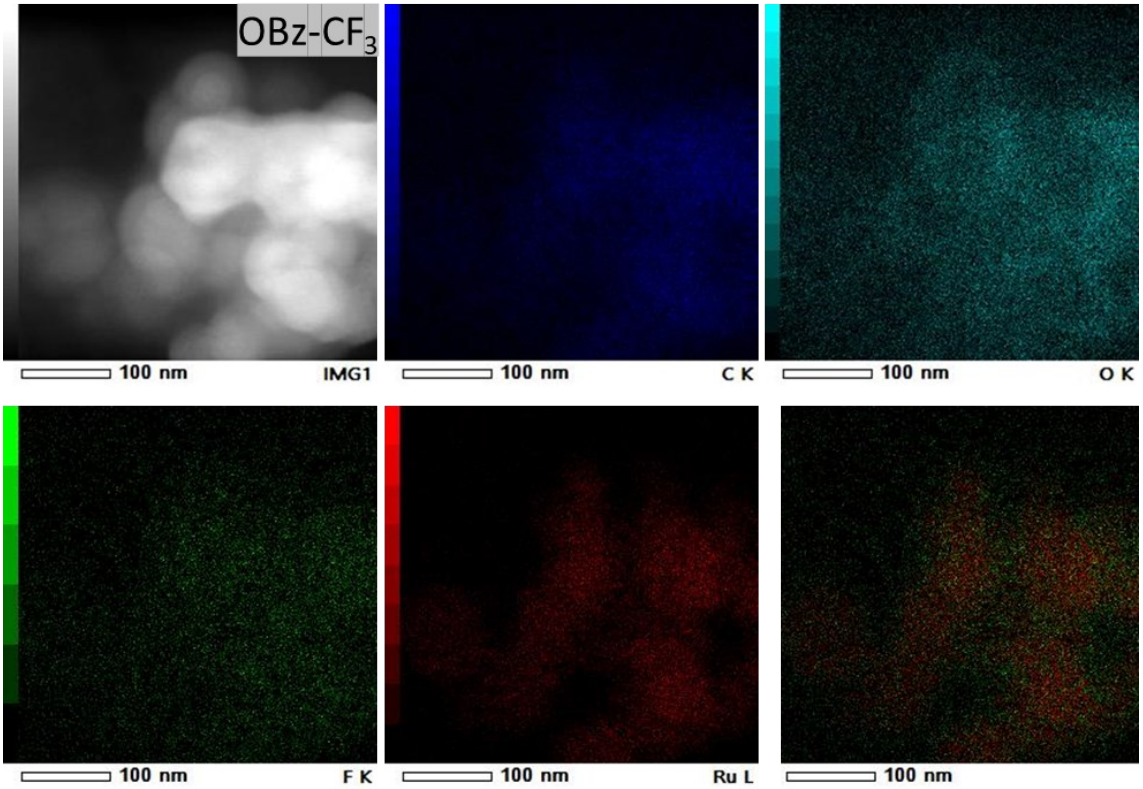

Figure S 35: A dark field STEM image of a representative particles of the OBz-CF_3 sample and corresponding EDS compositional maps of C, O, F and Ru and an overlay of F/Ru. Scale bars represent 100 nm. The bottom right image is an overlay of fluorine (green) and ruthenium (red). The images suggest the modulator to be preferentially located at the surface of the particles.

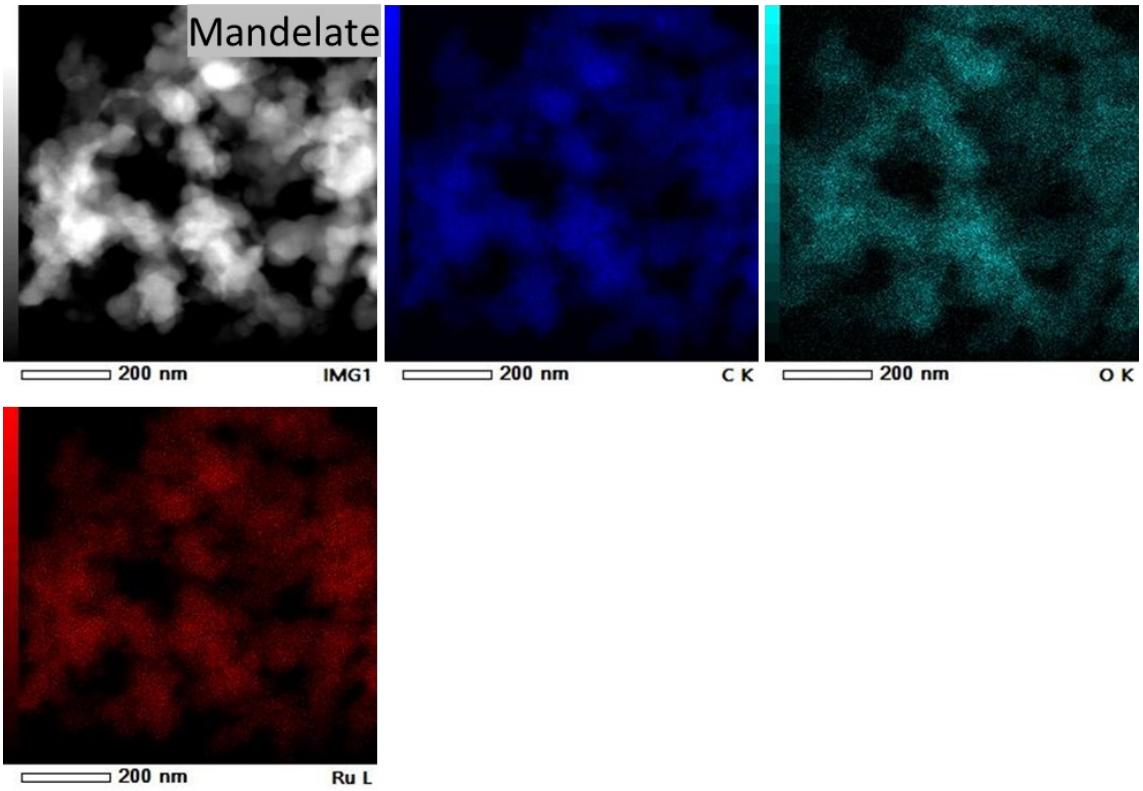

Figure S 36: A dark field STEM image of a representative particles of the mandelate-derived MOF sample and corresponding EDS compositional maps of C, O and Ru indicates a homogeneous elemental distribution. Scale bars represent 200 nm.

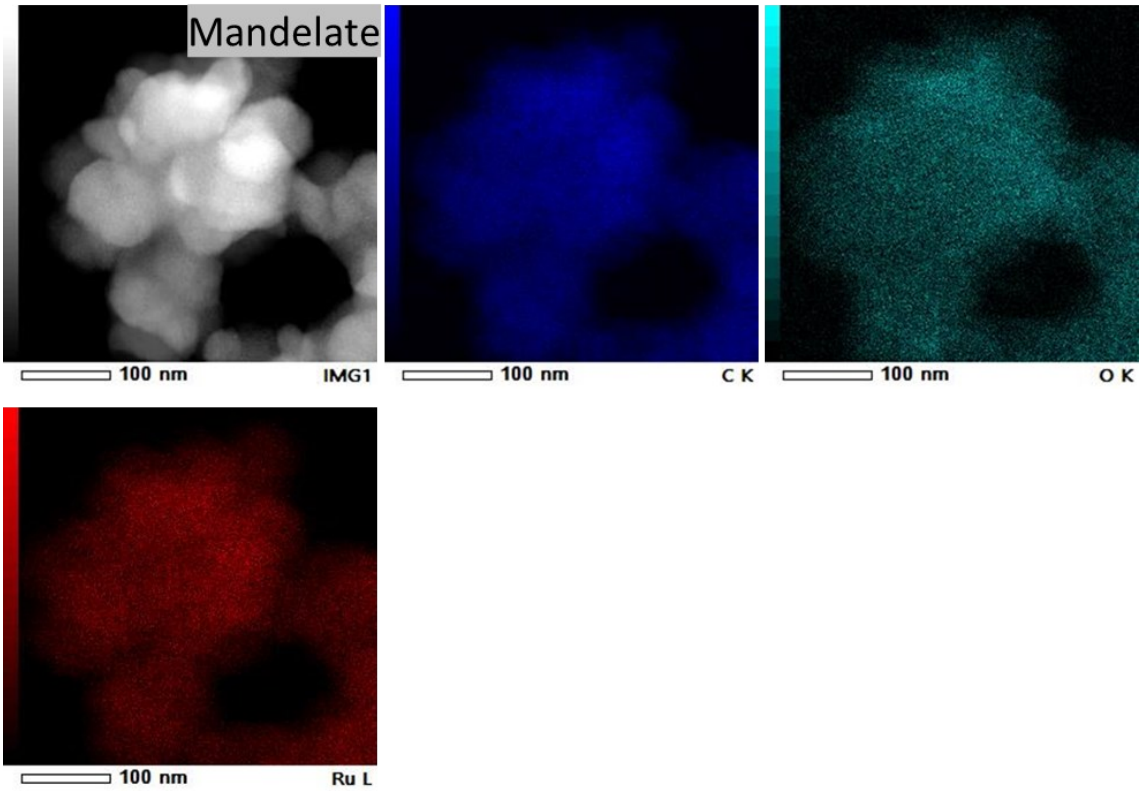

Figure S 37: A dark field STEM image of a representative particles of the mandelate-derived MOF sample and corresponding EDS compositional maps of C, O and Ru indicates a homogeneous elemental distribution. Scale bars represent 200 nm.

1. W. R. Heinz, T. Kratky, M. Drees, A. Wimmer, O. Tomanec, S. Günther, M. Schuster and R. A. Fischer, *Dalton Trans.*, 2019, **48**, 12031-12039.
2. A. J. Lindsay, G. Wilkinson, M. Motevalli and M. B. Hursthouse, *J. Chem. Soc., Dalton Trans.*, 1985, DOI: 10.1039/DT9850002321, 2321-2326.
3. R. W. Mitchell, A. Spencer and G. Wilkinson, *J. Chem. Soc., Dalton Trans.*, 1973, DOI: 10.1039/DT9730000846, 846-854.
4. F. A. Cotton, V. M. Miskowski and B. Zhong, *J. Am. Chem. Soc.*, 1989, **111**, 6177-6182.
5. V.F.Kuznetsov, H.Alper and G.P.A.Yap, CCDC 136234: Experimental Crystal Structure Determination, 2000, DOI: 10.5517/cc4krn2
6. A. J. Lindsay, G. Wilkinson, M. Motevalli and M. B. Hursthouse, *J. Chem. Soc., Dalton Trans.*, 1987, DOI: 10.1039/DT9870002723, 2723-2736.
7. M. Spohn, J. Strähle and W. Hiller, *Zeitschrift für Naturforschung*, 1986, **41b**, 541-547.
8. M. C. Barral, R. González-Prieto, R. Jiménez-Aparicio, J. L. Priego, M. R. Torres and F. A. Urbanos, *Inorg. Chim. Acta*, 2005, **358**, 217-221.
9. H. Miyasaka, N. Motokawa, R. Atsuumi, H. Kamo, Y. Asai and M. Yamashita, *Dalton Trans.*, 2011, **40**, 673-682.
10. Y. Sekine, K. H. Aliyah, T. Shimada, J. Zhang, W. Kosaka and H. Miyasaka, *Chem. Lett.*, 2018, **47**, 693-696.
11. D. S. Martin, R. A. Newman and L. M. Vlasnik, *Inorg. Chem.*, 1980, **19**, 3404-3407.
12. G. Vamvounis, J. F. Caplan, T. S. Cameron, K. N. Robertson and M. A. S. Aquino, *Inorg. Chim. Acta*, 2000, **304**, 87-98.
13. J. Liu, J. T. Culp, S. Natesakhawat, B. C. Bockrath, B. Zande, S. G. Sankar, G. Garberoglio and J. K. Johnson, *J. Phys. Chem. C*, 2007, **111**, 9305-9313.